Hanle-Zeeman redistribution matrix
I. Classical theory expressions in the laboratory frame

M. Sampoorna[1] and K. N. Nagendra

Indian Institute of Astrophysics, Koramangala Lay out, Bangalore 560 034, India

and

J. O. Stenflo

Institute of Astronomy, ETH Zurich, CH-8092 Zurich, Switzerland

ABSTRACT

Polarized scattering in spectral lines is governed by a 4×4 matrix that describes how the Stokes vector is scattered and redistributed in frequency and direction. Here we develop the theory for this redistribution matrix in the presence of magnetic fields of arbitrary strength and direction. This general magnetic field case is called the Hanle-Zeeman regime, since it covers both of the partially overlapping weak and strong-field regimes in which the Hanle and Zeeman effects dominate the scattering polarization. In this general regime the angle-frequency correlations that describe the so-called partial frequency redistribution (PRD) are intimately coupled to the polarization properties. We develop the theory for the PRD redistribution matrix in this general case and explore its detailed mathematical properties and symmetries for the case of a $J = 0 \rightarrow 1 \rightarrow 0$ scattering transition, which can be treated in terms of time-dependent classical oscillator theory. It is shown how the redistribution matrix can be expressed as a linear superposition of coherent and non-coherent parts, each of which contain the magnetic redistribution functions that resemble the well known Hummer type functions. We also show how the classical theory can be extended to treat atomic and molecular scattering transitions for any combinations of quantum numbers.

Subject headings: Redistribution Matrix: Polarization - Line formation: Partial Redistribution

---

[1]Joint Astronomy Program, Dept. of Physics, IISc, Bangalore-560 012; sampoorna@iiap.res.in

1. Introduction

The discovery of the extremely rich structuring of the Second Solar Spectrum (Stenflo & Keller 1996, 1997) opened the window to a new, previously unexplored territory with great diagnostic potential. This linearly polarized spectrum, which is formed by coherent scattering processes, has been mapped with high spectral resolution from the UV at $3160\,\text{Å}$ to the red at $6995\,\text{Å}$ (Gandorfer 2000, 2002, 2005), providing us with a wealth of new information both about the Sun and about the physics of spectral line formation in magnetized stellar atmospheres. The Second Solar Spectrum is modified by magnetic fields through the Hanle and Zeeman effects. The Hanle effect represents the magnetic modification of the scattering polarization. It is a coherency phenomenon and responds to weak fields, when the Zeeman splitting is comparable to the small damping width of line transitions. The usual Zeeman-effect polarization, on the other hand, is produced by stronger fields, when the Zeeman splitting gets comparable to the much larger Doppler width of the line. A further difference between the two effects is that the Hanle effect is sensitive to spatially unresolved turbulent fields with zero net magnetic flux, while the Zeeman effect is blind to such fields (due to its different symmetry properties). The two effects therefore nicely complement each other (cf. Stenflo 1994).

Many of the strongest and most conspicuous lines in the Second Solar Spectrum are strong lines that are formed rather high, often in the chromosphere above the temperature minimum. From standard, unpolarized and non-magnetic line-formation theory such lines are known to be formed under conditions that are very far from local thermodynamic equilibrium. They are characterized by broad damping wings surrounding a Doppler core. Doppler shifts in combination with collisions cause photons that are absorbed at a given frequency to be redistributed in frequency across the line profile in a complex way during the scattering process. Two idealized, limiting cases to describe this redistribution are "frequency coherence" and "complete redistribution", but the general theory that properly combines these two limiting cases goes under the name "partial frequency redistribution". Strong lines can only be properly modeled when PRD is taken into account.

The complexity of the redistribution problem escalates when we include polarization and magnetic fields, since the previously unpolarized scalar redistribution function becomes a 4×4 redistribution matrix that describes how the Stokes 4-vector is redistributed in both frequency and angle. In the absence of magnetic fields the frequency redistribution factorizes out from the polarization properties, which can be described by a frequency-independent 4×4 phase matrix. Such non-magnetic but polarized PRD has been applied to describe the polarized line profile of Ca I $4227\,\text{Å}$ (Saliba 1985; Faurobert-Scholl 1992) and later to model other strong lines in the Second Solar Spectrum (Fluri et al. 2003a; Holzreuter et al. 2005),

like Na I D_2 5890 Å, and other important lines such as Sr II 4078 Å, and Cr I 3594 Å.

To exploit these strong lines for magnetic-field diagnostics we need however to go one step further, namely to develop the theory for PRD in the presence of magnetic fields of arbitrary strengths. This is the aim of the present paper. In the presence of magnetic fields we can no longer factorize the polarization and frequency redistribution problem, but they get deeply intertwined. This naturally increases the complexity of the problem, but this complexity also has a rich structure with many symmetries.

The general concepts of theory of PRD were first developed for the scalar problem of non-polarized scattering (cf. Mihalas 1978). The theory of PRD from a classical perspective was originally introduced by Zanstra (1941), who addressed the issue of collisions on non-magnetic frequency redistribution in resonance lines. Stenflo (1994, 1996, 1998) has developed a modern approach to the classical oscillator theory and applied it to atomic line transitions. His method can handle light scattering on atomic energy levels in the presence of arbitrary magnetic fields and various kinds of collisions (treated approximately). This classical framework was further extended by Bommier & Stenflo (1999, hereafter called BS99) to handle PRD effects in the presence of arbitrary magnetic fields and collisions. Recently, Lin et al. (1998) have proposed a classical theory of the Hanle effect (similar to that of Stenflo 1994), to explain the polarization of He I 10830 Å line observed in a solar filament. This classical theory has been extended by Lin & Casini (2000) to derive the polarization properties of the coronal forbidden emission lines, which arise from magnetic dipole (M1) transitions.

The quantum mechanical framework for the problem of atomic line scattering was developed by Weisskopf (1933), Wooley (1938), Henyey (1940), Hummer (1962), Lamb & ter Haar (1971), House (1971), Omont et al. (1972, 1973), Heinzel (1981), Cooper et al. (1982), Landi Degl'Innocenti (1983, 1984), Domke & Hubeny (1988), Streater et al. (1988), Landi Degl'Innocenti et al. (1997), Bommier (1997a,b, 1999, 2003), Casini & Manso Sainz (2005). See the reviews by Hubeny (1985); Nagendra (2003) for a historical development of the PRD formulations, and Trujillo Bueno (2003); Uitenbroek (2003) for applications in Astrophysical line formation theory, and Nagendra et al. (2002, 2003, and papers cited therein), and Fluri et al. (2003b) for powerful numerical methods of solving the relevant line transfer problem, of varying complexity.

The theory developed in BS99 solved the time-dependent oscillator equation in combination with a classical model for collisions (see Stenflo 1994, ch. 10). This gives self-consistent and non-perturbative expressions for the polarized partial frequency redistribution matrix, in the presence of magnetic fields of arbitrary strength and direction in the atomic frame. The explicit form of the redistribution matrix in the laboratory frame was not given. BS99

hints at the way to arrive at such expressions, which are needed, when the generalized Hanle-Zeeman redistribution matrix is to be used in a radiative line transfer code.

When we here use the term "Hanle-Zeeman", we mean the full field-strength regime, from zero field to completely split lines. This general case contains many sub-regimes, which only become distinct from each other if one makes idealizations, to deal with each separately. We do not do any such idealizations here, so in this general case, the sub-regimes partially overlap or gradually flow into each other. The Hanle effect has three sub-regimes: (i) Very weak fields, when the field dependence can be disregarded, and the scattering behaves like the non-magnetic case. (ii) Weak to intermediate fields, when the scattering polarization depends on both the strength and direction of the field. This is what is most often referred to as the "Hanle regime". (iii) Saturated Hanle regime, when the fields are so strong that the scattering polarization becomes insensitive to the field strength, but still depends on the field direction. This saturated Hanle regime is what applies to the coronal forbidden lines. The saturation occurs when the Zeeman splitting becomes much larger than the damping width. Even in this saturated regime the Zeeman splitting can remain much smaller than the Doppler width, as it does in the case of the coronal forbidden lines. When the Zeeman splitting is no longer too small in comparison with the Doppler width, then ordinary Zeeman-effect polarization starts to show up. The field strengths for which this occurs depend on the relative prominence of scattering polarization and the polarimetric sensitivity of the instrument. While the Hanle and Zeeman effects show relative dominance in different regimes, they fundamentally overlap over the whole field strength regime.

In this paper we derive an explicit form of the Hanle-Zeeman redistribution matrix in the laboratory frame, for the special case of a normal Zeeman triplet, in a co-ordinate system in which the polar z axis is oriented along the magnetic field (cf. Fig. 1). This choice of geometry does not limit the applicability of the theory, since the redistribution matrix for an arbitrary field direction can be obtained by first choosing a system with the z axis along the magnetic field, and then applying Mueller rotation matrices to obtain the redistribution matrix for any other system with an arbitrary orientation of its z axis.

In Section 2, starting from the atomic frame expression for the ensemble averaged coherency matrix given in BS99, we derive the corresponding expression in the laboratory frame. In Section 3 we present the analytical form of the Hanle-Zeeman redistribution matrix. The magnetic redistribution basis functions that we encounter in Sect. 2 (see also Bommier 1997b) are numerically studied in Sect. 4, because the total scattering probability essentially depends on their angular and frequency dependence. The scattered Stokes vector can be interpreted using the properties of these basis functions. The extension of the classical theory presented in Sections 2 and 3, to treat atomic and molecular scattering for any

combination of quantum numbers is discussed in Sect. 5. Concluding remarks are given in Sect. 6.
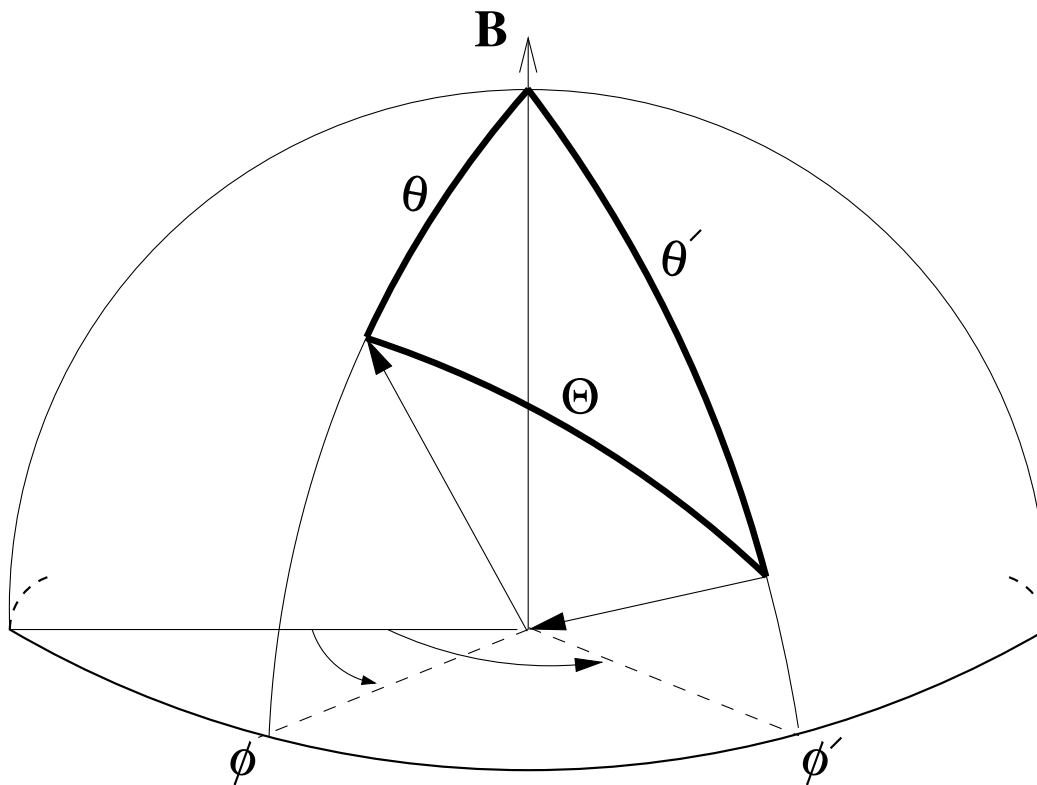
Fig. 1.— The geometry showing the scattering process in a co-ordinate system where the polar z axis is oriented along the magnetic field. (θ', ϕ') refer to the incident ray, (θ, ϕ) to the scattered ray. Θ is the scattering angle.

2.   Coherency Matrix

The time dependent solution $r_q(t, \xi')$, of the oscillator equation, which describes the motion of a particle with charge $-e$ and mass m in a central Coulomb potential, subject to an external magnetic field $\mathbf{B}$ and an external oscillating electric field $\mathbf{E}'$, is given by (see Eqs. (16) - (18) of BS99)

$$r_q(t, \xi') = r_{q,\,\mathrm{stat}}(t, \xi') + C r_{q,\,\mathrm{trans}}(t, \xi')\, e^{i\delta}, \tag{1}$$

where

$$r_{q,\,\mathrm{stat}}(t, \xi') = \frac{1}{\pi} \frac{e^{-2\pi i \xi' t}}{\xi' - (\nu_0 - q\nu_L - i\gamma/4\pi)}, \tag{2}$$

represents the stationary solution, and

$$r_{q,\,\mathrm{trans}}(t, \xi') = \frac{1}{\pi} \frac{e^{-2\pi i(\nu_0 - q\nu_L - i\gamma/4\pi)t}}{\xi' - (\nu_0 - q\nu_L - i\gamma/4\pi)}, \tag{3}$$

represents the transitory solution for a free, damped oscillator. C and δ represent the amplitude and phase of the oscillator. ξ' is the frequency of the incident radiation in the atomic frame. ν_0, ν_L are the frame independent line center frequency and Larmor frequency, respectively.

The spectral properties of the scattered radiation are obtained by taking the Fourier transform of $r_q(t, \xi')$, defined as

$$\tilde{r}_q(\xi, \xi') = \int_{-\infty}^{+\infty} r_q(t, \xi')\, e^{2\pi i \xi t}\, dt, \tag{4}$$

where ξ is the frequency of the scattered radiation in the atomic frame. The ensemble average of bilinear products, also called the coherency matrix, is denoted by $\langle \tilde{r}_q \tilde{r}_{q'}^* \rangle$ and contains all the frequency information, including the partial redistribution effects that correlate the incident and scattered frequencies with each other. The ensemble average is performed to include the random phase shifts that arise due to random phase destroying collisions.

2.1.   Redistribution in the Atomic Frame

The expression for the ensemble averaged coherency matrix $\langle \tilde{r}_q \tilde{r}_{q'}^* \rangle$ is given in BS99, in the atomic frame (see Eqs. (27), (35) and (39) of BS99) as

$$\begin{aligned}
\langle \tilde{r}_q \tilde{r}_{q'}^* \rangle \quad \sim \quad & A \cos\beta_{q-q'}\, e^{i\beta_{q-q'}} \Phi_{qq'}^{\gamma+\gamma_c}(\xi')\delta(\xi - \xi') + B \cos\beta_{q-q'} \cos\alpha_{q-q'}\, e^{i(\beta_{q-q'}+\alpha_{q-q'})} \\
& \times \Phi_{qq'}^{\gamma+\gamma_c}(\xi')\Phi_{qq'}^{\gamma+\gamma_c}(\xi),
\end{aligned} \tag{5}$$

where $\beta_{q-q'}$, $\alpha_{q-q'}$ are Hanle angles defined as

$$\tan \beta_{q-q'} = \frac{(q-q')2\pi\nu_L}{\gamma + \gamma_c}, \tag{6}$$

and

$$\tan \alpha_{q-q'} = \frac{(q-q')2\pi\nu_L}{\gamma + \gamma_c/2}, \tag{7}$$

with γ being a sum of radiative and inelastic collisional damping constants and γ_c the elastic collisional damping rate. q, q' take values 0, ± 1. The effect of Hanle angle $\beta_{q-q'}$ vanishes in the line core due to cancellation between contributions from stationary and transitory solutions. Thereby only the Hanle angle $\alpha_{q-q'}$ remains operative in the line core, and causes depolarization via the $\cos \alpha_{q-q'}$ factor, and rotation of the plane of polarization through the $e^{i\alpha_{q-q'}}$ factor. In the line wings the Hanle effect from both $\alpha_{q-q'}$ and $\beta_{q-q'}$ vanishes as shown in Stenflo (1998).

The generalized profile function is defined as

$$\Phi_{qq'}^{\gamma+\gamma_c}(\xi) = \frac{1}{2}\left[\Phi_{\gamma+\gamma_c}(\nu_q - \xi) + \Phi_{\gamma+\gamma_c}^*(\nu_{q'} - \xi)\right], \tag{8}$$

with the profile function given by

$$\Phi_{\gamma+\gamma_c}(\nu_q - \xi) = \frac{2/\pi i}{\nu_0 - q\nu_L - \xi - i(\gamma + \gamma_c)/4\pi}, \tag{9}$$

where $\nu_q = \nu_0 - q\nu_L$. We can rewrite Eq. (9) as

$$\Phi_{\gamma+\gamma_c}(\nu_q - \xi) = \frac{1}{\pi}\frac{\delta_w - i(\nu_0 - q\nu_L - \xi)}{\delta_w^2 + (\nu_0 - q\nu_L - \xi)^2}, \tag{10}$$

where $\delta_w = (\gamma + \gamma_c)/4\pi$.

A and B in Eq. (5) are branching ratios between stationary and transitory solutions, determined by probability arguments and normalization. The stationary solution is the source of frequency–coherent scattering. The branching ratio A for frequency–coherent process is (see Eq. (40) of BS99)

$$A = \frac{\Gamma_{\rm R}}{\Gamma_{\rm R} + \Gamma_{\rm I} + \Gamma_{\rm E}}, \tag{11}$$

where $\Gamma_{\rm R}$ is radiative rate, while $\Gamma_{\rm I}$ and $\Gamma_{\rm E}$ are inelastic and elastic collision rates, respectively.

The transitory solution is the source of complete redistribution. Thus branching ratio B represents the fraction of the scattering processes for which the atom is subject to elastic

collisions that destroy the frequency–coherence but not the atomic polarization (the $2K$-multipole). Hence B is given by (see Eq. (41) of BS99)

$$B = \frac{\Gamma_{\rm E} - D^{(K)}}{\Gamma_{\rm R} + \Gamma_{\rm I} + \Gamma_{\rm E}} \frac{\Gamma_{\rm R}}{\Gamma_{\rm R} + \Gamma_{\rm I} + D^{(K)}}, \tag{12}$$

where $D^{(K)}$ is the rate of destruction of the $2K$-multipole, with $K = 0, 1, 2$ (note that $D^{(0)} = 0$). We note that $\Gamma_{\rm R} + \Gamma_{\rm I} = \gamma$, $\Gamma_{\rm E} = \gamma_c$, and $D^{(K)} = \gamma_c/2$ in the classical theory (see Eqs. (31)-(33) of BS99).

Substituting Eq. (8) into Eq. (5), we obtain

$$\begin{aligned}
\langle \tilde{r}_q \tilde{r}_{q'}^* \rangle \sim\ & A \cos \beta_{q-q'}\, e^{i\beta_{q-q'}} \frac{1}{2} [\Phi'_{\gamma+\gamma_c}(\nu_q - \xi')\delta(\xi - \xi') + \Phi'^*_{\gamma+\gamma_c}(\nu_{q'} - \xi')\delta(\xi - \xi')] \\
& + B \cos \beta_{q-q'} \cos \alpha_{q-q'}\, e^{i(\beta_{q-q'} + \alpha_{q-q'})} \frac{1}{4} [\Phi'_{\gamma+\gamma_c}(\nu_q - \xi')\Phi_{\gamma+\gamma_c}(\nu_q - \xi) \\
& + \Phi'^*_{\gamma+\gamma_c}(\nu_{q'} - \xi')\Phi_{\gamma+\gamma_c}(\nu_q - \xi) + \Phi'_{\gamma+\gamma_c}(\nu_q - \xi')\Phi^*_{\gamma+\gamma_c}(\nu_{q'} - \xi) \\
& + \Phi'^*_{\gamma+\gamma_c}(\nu_{q'} - \xi')\Phi^*_{\gamma+\gamma_c}(\nu_{q'} - \xi)].
\end{aligned} \tag{13}$$

Clearly terms in the square brackets represent the well known type II (in first square bracket) and III (in second square bracket) atomic frame redistribution functions of Hummer (1962). However, the essential difference is that we now have magnetically shifted frequencies (for both incoming and outgoing photons), and the profile functions are complex Lorentzians. The complex profile functions automatically take into account the magneto-optical effects (imaginary part) and the absorption or emission effects (real part). The radiative transfer equation is always formulated in the laboratory frame. Therefore the redistribution matrices that appear in the scattering integral should refer to the laboratory frame. Hence there is a need to transform them from the atomic frame to the laboratory frame.

2.2. Doppler Redistribution in the Laboratory Frame

The effect of the Doppler shifts (introduced by the motion of scattering atoms relative to the fixed laboratory frame) is taken into account by convolving the atomic frame redistribution function with a velocity distribution of the scattering atoms, which is conventionally assumed to be Maxwellian (see Mihalas 1978, Eq. (13.13), p.417). Thus when going from the atomic frame to the laboratory frame, we first have to replace ξ' and ξ by their Doppler shifted values, related through

$$\begin{aligned}
\xi &= \nu - \nu_0(\mathbf{v} \cdot \mathbf{n})/c, \\
\xi' &= \nu' - \nu_0(\mathbf{v} \cdot \mathbf{n}')/c,
\end{aligned} \tag{14}$$

where $\mathbf{v}$ is the velocity vector, and c is the speed of light. ν and ν' are outgoing and incoming frequencies relative to the laboratory frame. $\mathbf{n}$ and $\mathbf{n}'$ are the directions of the outgoing and incoming radiation. We introduce the dimensionless quantities

$$x = \frac{\nu_0 - \nu}{\Delta\nu_{\mathrm{D}}}; \quad v_q = x - \frac{q\nu_L}{\Delta\nu_{\mathrm{D}}}; \quad a = \frac{\delta_w}{\Delta\nu_{\mathrm{D}}}, \tag{15}$$

which are respectively, the emission frequency, magnetic shift, and damping parameter. $\Delta\nu_{\mathrm{D}}$ is the Doppler width.

From Eq. (13) it is clear that each term in the square bracket can be independently transformed to the laboratory frame. Following Mihalas (1978, ch. 13), one can easily obtain (after some algebra) the ensemble averaged coherency matrix in the laboratory frame as

$$\begin{aligned}
\langle \tilde{r}_q \tilde{r}_{q'}^* \rangle \quad \sim \quad & A\cos\beta_{q-q'}\, e^{i\beta_{q-q'}} \frac{1}{2}[R_{\mathrm{II}}^q(x,\, \mathbf{n};\, x',\, \mathbf{n}') + R_{\mathrm{II}}^{q'\,*}(x,\, \mathbf{n};\, x',\, \mathbf{n}')] + B\cos\beta_{q-q'} \\
& \times \cos\alpha_{q-q'}\, e^{i(\beta_{q-q'}+\alpha_{q-q'})} \frac{1}{4}[R_{\mathrm{III}}^{qq}(x,\, \mathbf{n};\, x',\, \mathbf{n}') + R_{\mathrm{III}}^{q'\,*\,q}(x,\, \mathbf{n};\, x',\, \mathbf{n}') \\
& + R_{\mathrm{III}}^{qq'\,*}(x,\, \mathbf{n};\, x',\, \mathbf{n}') + R_{\mathrm{III}}^{q'\,q'\,*}(x,\, \mathbf{n};\, x',\, \mathbf{n}')],
\end{aligned} \tag{16}$$

where

$$R_{\mathrm{II}}^q(x,\, \mathbf{n};\, x',\, \mathbf{n}') = \frac{1}{\pi\sin\Theta} \exp\left\{ -\left[\frac{x-x'}{2\sin(\Theta/2)}\right]^2 \right\} \mathcal{H}\left(\frac{a}{\cos(\Theta/2)},\, \frac{v_q + v_q'}{2\cos(\Theta/2)} \right), \tag{17}$$

and

$$R_{\mathrm{III}}^{qq'}(x,\, \mathbf{n};\, x',\, \mathbf{n}') = \frac{1}{\pi^2\sin\Theta} \int_{-\infty}^{+\infty} du\, e^{-u^2} \left[\frac{a - i(v_q' - u)}{a^2 + (v_q' - u)^2} \right] \mathcal{H}\left(\frac{a}{\sin\Theta},\, \frac{v_{q'}}{\sin\Theta} - u\cot\Theta \right). \tag{18}$$

The symbol $R_{\mathrm{III}}^{q'\,*\,q}(x,\, \mathbf{n};\, x',\, \mathbf{n}')$ stands for complex conjugation only on the incoming profile (i.e., on the complex Lorentzian in Eq. (18) — the term in the square bracket), while the symbol $R_{\mathrm{III}}^{q'q'\,*}(x,\, \mathbf{n};\, x',\, \mathbf{n}')$ stands for complex conjugation on both the incoming and outgoing profiles. (Note: a prime on v means incoming radiation, while the absence of a prime on v means outgoing radiation. This convention does not hold for indices q and q'.) In Eqs. (17) and (18), Θ is the scattering angle (the angle between incident and scattered ray – cf. Fig. 1), and we have introduced the complex function

$$\mathcal{H}(a,\, x) = H(a,\, x) - 2iF(a,\, x), \tag{19}$$

with the Voigt and Faraday-Voigt functions defined as

$$\begin{aligned}
H(a,\, x) &= \frac{a}{\pi} \int_{-\infty}^{+\infty} \frac{e^{-y^2}dy}{(x-y)^2 + a^2}, \\
F(a,\, x) &= \frac{1}{2\pi} \int_{-\infty}^{+\infty} \frac{(x-y)e^{-y^2}dy}{(x-y)^2 + a^2}.
\end{aligned} \tag{20}$$

From Eqs. (17) and (18) we can construct the real valued mathematical basis functions, which we call the magnetic redistribution functions (hereafter magnetic RF). They are given by

$$R_{\mathrm{II,\,H}}^{q}(x,\,x',\,\Theta) = \frac{1}{\pi \sin \Theta} \exp \left\{ - \left[\frac{x - x'}{2 \sin(\Theta/2)} \right]^{2} \right\} H \left(\frac{a}{\cos(\Theta/2)},\, \frac{v_{q} + v_{q}'}{2 \cos(\Theta/2)} \right), \quad (21)$$

$$R_{\mathrm{II,\,F}}^{q}(x,\,x',\,\Theta) = \frac{1}{\pi \sin \Theta} \exp \left\{ - \left[\frac{x - x'}{2 \sin(\Theta/2)} \right]^{2} \right\} 2F \left(\frac{a}{\cos(\Theta/2)},\, \frac{v_{q} + v_{q}'}{2 \cos(\Theta/2)} \right), \quad (22)$$

for redistribution of type II, which depends only on q and

$$\begin{aligned} R_{\mathrm{III,\,HH}}^{qq'}(x,\,x',\,\Theta) &= \frac{1}{\pi^{2} \sin \Theta} \int_{-\infty}^{+\infty} du\, e^{-u^{2}} \left[\frac{a}{a^{2} + (v_{q}' - u)^{2}} \right] \\ &\quad \times H \left(\frac{a}{\sin \Theta},\, \frac{v_{q'}}{\sin \Theta} - u \cot \Theta \right), \end{aligned} \quad (23)$$

$$\begin{aligned} R_{\mathrm{III,\,HF}}^{qq'}(x,\,x',\,\Theta) &= \frac{1}{\pi^{2} \sin \Theta} \int_{-\infty}^{+\infty} du\, e^{-u^{2}} \left[\frac{a}{a^{2} + (v_{q}' - u)^{2}} \right] \\ &\quad \times 2F \left(\frac{a}{\sin \Theta},\, \frac{v_{q'}}{\sin \Theta} - u \cot \Theta \right), \end{aligned} \quad (24)$$

$$\begin{aligned} R_{\mathrm{III,\,FH}}^{qq'}(x,\,x',\,\Theta) &= \frac{1}{\pi^{2} \sin \Theta} \int_{-\infty}^{+\infty} du\, e^{-u^{2}} \left[\frac{(v_{q}' - u)}{a^{2} + (v_{q}' - u)^{2}} \right] \\ &\quad \times H \left(\frac{a}{\sin \Theta},\, \frac{v_{q'}}{\sin \Theta} - u \cot \Theta \right), \end{aligned} \quad (25)$$

and

$$\begin{aligned} R_{\mathrm{III,\,FF}}^{qq'}(x,\,x',\,\Theta) &= \frac{1}{\pi^{2} \sin \Theta} \int_{-\infty}^{+\infty} du\, e^{-u^{2}} \left[\frac{(v_{q}' - u)}{a^{2} + (v_{q}' - u)^{2}} \right] \\ &\quad \times 2F \left(\frac{a}{\sin \Theta},\, \frac{v_{q'}}{\sin \Theta} - u \cot \Theta \right), \end{aligned} \quad (26)$$

for redistribution of type III, which depends on both q and q'. We note that $R_{\mathrm{II,\,H}}^{0}$ and $R_{\mathrm{III,\,HH}}^{00}$ (dropping the arguments for brevity), are nothing but the well known R_{II} and R_{III} scalar redistribution functions of Hummer (1962) in the laboratory frame. It will be shown in Sect. 4, that the overall behavior of the magnetic RF is similar to the non-magnetic RF of Hummer, except for changes caused by Zeeman frequency shifts (appearance of several magnetic components: (2×3) in R_{II} type scattering; (4×9) in R_{III} type scattering).

For notational simplification, we now introduce the following auxiliary functions (which are linear combination of magnetic RF introduced above),

$$h_{qq'}^{\mathrm{II}} = \frac{1}{2} \left[R_{\mathrm{II,\,H}}^{q} + R_{\mathrm{II,\,H}}^{q'} \right], \tag{27}$$

$$f_{qq'}^{\mathrm{II}} = \frac{1}{2} \left[R_{\mathrm{II,\,F}}^{q'} - R_{\mathrm{II,\,F}}^{q} \right], \tag{28}$$

for type II functions. For type III functions, we define a complex h-function:

$$h_{qq'}^{\mathrm{III}} = \Re[h_{qq'}^{\mathrm{III}}] + i\Im[h_{qq'}^{\mathrm{III}}], \tag{29}$$

where the real ($\Re$) and imaginary ($\Im$) parts are defined through

$$\Re[h_{qq'}^{\mathrm{III}}] = \frac{1}{4} \left[R_{\mathrm{III,\,HH}}^{q'q'} + R_{\mathrm{III,\,HH}}^{q'q} + R_{\mathrm{III,\,HH}}^{qq'} + R_{\mathrm{III,\,HH}}^{qq} \right], \tag{30}$$

$$\Im[h_{qq'}^{\mathrm{III}}] = \frac{1}{4} \left[R_{\mathrm{III,\,FH}}^{q'q'} + R_{\mathrm{III,\,FH}}^{q'q} - R_{\mathrm{III,\,FH}}^{qq'} - R_{\mathrm{III,\,FH}}^{qq} \right], \tag{31}$$

which are expressed in terms of HH and FH type of basis functions respectively. An analogous expression can be written for the complex f-function:

$$f_{qq'}^{\mathrm{III}} = \Re[f_{qq'}^{\mathrm{III}}] + i\Im[f_{qq'}^{\mathrm{III}}], \tag{32}$$

where the real and imaginary parts are now defined through

$$\Re[f_{qq'}^{\mathrm{III}}] = \frac{1}{4} \left[R_{\mathrm{III,\,HF}}^{q'q'} - R_{\mathrm{III,\,HF}}^{q'q} + R_{\mathrm{III,\,HF}}^{qq'} - R_{\mathrm{III,\,HF}}^{qq} \right], \tag{33}$$

$$\Im[f_{qq'}^{\mathrm{III}}] = \frac{1}{4} \left[R_{\mathrm{III,\,FF}}^{q'q'} - R_{\mathrm{III,\,FF}}^{q'q} - R_{\mathrm{III,\,FF}}^{qq'} + R_{\mathrm{III,\,FF}}^{qq} \right]. \tag{34}$$

We note that $f_{qq'}^{\mathrm{II}}$, $\Im[h_{qq'}^{\mathrm{III}}]$, $f_{qq'}^{\mathrm{III}}$ are non-zero only when $q \neq q'$. The auxiliary quantities defined above satisfy the following symmetry relations:

$$\begin{aligned} h_{qq'}^{\mathrm{II}} &= h_{q'q}^{\mathrm{II}}; & f_{qq'}^{\mathrm{II}} &= -f_{q'q}^{\mathrm{II}}, \\ h_{qq'}^{\mathrm{III}} &= h_{q'q}^{\mathrm{III}\,*}; & f_{qq'}^{\mathrm{III}} &= -f_{q'q}^{\mathrm{III}\,*}. \end{aligned} \tag{35}$$

Using Eqs. (27) - (34), we can rewrite Eq. (16) as

$$\begin{aligned} \langle \tilde{r}_q \tilde{r}_{q'}^* \rangle \quad \sim \quad & A \cos\beta_{q-q'}\, e^{i\beta_{q-q'}} [h_{qq'}^{\mathrm{II}} + i f_{qq'}^{\mathrm{II}}] + B \cos\beta_{q-q'} \cos\alpha_{q-q'}\, e^{i(\beta_{q-q'} + \alpha_{q-q'})} \\ & \times \left\{ \Re[h_{qq'}^{\mathrm{III}}] - \Im[f_{qq'}^{\mathrm{III}}] + i\left(\Im[h_{qq'}^{\mathrm{III}}] + \Re[f_{qq'}^{\mathrm{III}}] \right) \right\}. \end{aligned} \tag{36}$$

3.   Analytical Form of the Hanle-Zeeman Redistribution Matrix

For clarity and compactness we have derived analytical expression for the Hanle-Zeeman redistribution matrix for the simpler case of a normal Zeeman triplet ($J = 0 \rightarrow 1 \rightarrow 0$ scattering transition), and for a co-ordinate system in which the polar axis is along the magnetic field. Fig. 1 shows the corresponding scattering geometry. The incident ray makes an angle θ' and azimuth ϕ' with respect to field direction, while outgoing ray makes an angle θ and azimuth ϕ. It is however possible to compute the redistribution matrix for arbitrary orientations of vector magnetic fields by using transformation matrices.

The Mueller scattering matrix $\hat{\mathbf{M}}$ that describes scattering of the Stokes vector is readily obtained from the coherency matrix (see Eq. (10) of BS99), using the expression

$$\hat{\mathbf{M}} = \hat{\mathbf{T}} \left(\hat{w} \otimes \hat{w}^* \right) \hat{\mathbf{T}}^{-1}, \tag{37}$$

where $\hat{w}$ is the Jones scattering matrix. For explicit expressions of $(\hat{w} \otimes \hat{w}^*)$ and the purely mathematical transformation matrices $\hat{\mathbf{T}}$ and $\hat{\mathbf{T}}^{-1}$, see Stenflo (1998, Eqs. (9) and (10)).

The elements of the Jones scattering matrix are given by (see Eq. (8) of BS99)

$$w_{\alpha\beta} \sim \sum_q \left[\frac{r_q(t, \omega')}{E'_{q, 0}} \right] \varepsilon_q^{\alpha *} \varepsilon_q^{\beta}, \tag{38}$$

where $E'_{q, 0}$ is the amplitude of the qth spherical component of incoming monochromatic plane wave, and $\varepsilon_q^{\alpha, \beta}$ are geometrical factors for the outgoing (α) and incoming (β) radiation, respectively. These geometrical factors are given by

$$\varepsilon_0^1 = -\sin\theta; \quad \varepsilon_\pm^1 = \mp \frac{\mu}{\sqrt{2}} e^{\pm i\phi},$$
$$\varepsilon_0^2 = 0; \quad \varepsilon_\pm^2 = -\frac{i}{\sqrt{2}} e^{\pm i\phi}, \tag{39}$$

for the outgoing radiation, with $\mu = \cos\theta$ (see Stenflo 1994, page 57). For the incoming radiation we simply replace (θ, ϕ) by (θ', ϕ'), in the above equations.

The tensor product $(\hat{w} \otimes \hat{w}^*)$, requires the construction of bilinear products $w_{\alpha\beta} w^*_{\alpha'\beta'}$, given by

$$w_{\alpha\beta} w^*_{\alpha'\beta'} = \sum_{qq'} \left[\frac{r_q(t, \omega') r^*_{q'}(t, \omega')}{E'_{q, 0} E'^*_{q', 0}} \right] \varepsilon_q^{\alpha *} \varepsilon_{q'}^{\alpha'} \varepsilon_q^{\beta} \varepsilon_{q'}^{\beta' *}. \tag{40}$$

Next we replace the term in the square bracket by the ensemble average $\langle \tilde{r}_q \tilde{r}^*_{q'} \rangle$, in order to take into account the collisions (see Sect. 2). Thus Eq. (40) becomes

$$w_{\alpha\beta} w^*_{\alpha'\beta'} = \sum_{qq'} \langle \tilde{r}_q \tilde{r}^*_{q'} \rangle \varepsilon_q^{\alpha *} \varepsilon_{q'}^{\alpha'} \varepsilon_q^{\beta} \varepsilon_{q'}^{\beta' *}. \tag{41}$$

Therefore the Mueller matrix $\hat{\mathbf{M}}$ can be calculated using Eqs. (36), (37), (39), and (41). The Hanle-Zeeman redistribution matrix is then given by

$$\hat{\mathbf{R}}(x,\ \mathbf{n};\ x',\ \mathbf{n}') = \frac{3}{2}\,\hat{\mathbf{M}}, \tag{42}$$

where 3/2 is the normalization constant (see Eq. (8.38) of Stenflo 1994).

We can now write the final expression for the Hanle-Zeeman grand redistribution matrix as

$$\hat{\mathbf{R}}(x,\ \mathbf{n};\ x',\ \mathbf{n}') = \hat{\mathbf{R}}^{\mathrm{II}}(x,\ \mathbf{n};\ x',\ \mathbf{n}') + \hat{\mathbf{R}}^{\mathrm{III}}(x,\ \mathbf{n};\ x',\ \mathbf{n}'), \tag{43}$$

where

$$\hat{\mathbf{R}}^{\mathrm{II}}(x,\ \mathbf{n};\ x',\ \mathbf{n}') = A\hat{\mathbf{M}}_{\mathrm{II}}, \tag{44}$$

$$\hat{\mathbf{R}}^{\mathrm{III}}(x,\ \mathbf{n};\ x',\ \mathbf{n}') = B\hat{\mathbf{M}}_{\mathrm{III}}, \tag{45}$$

with

$$
\begin{aligned}
\hat{\mathbf{M}}_{\mathrm{II}} =\ & \frac{3}{4}\,[c_{00}^{\mathrm{II}}\hat{\mathbf{C}}_0^0 + \frac{1}{2}(c_{11}^{\mathrm{II}} + c_{-1-1}^{\mathrm{II}})\hat{\mathbf{C}}_+^0 + \frac{1}{2}(c_{11}^{\mathrm{II}} - c_{-1-1}^{\mathrm{II}})\hat{\mathbf{C}}_-^0 + c_{1-1}^{\mathrm{II}}\hat{\mathbf{C}}_+^2 + s_{1-1}^{\mathrm{II}}\hat{\mathbf{S}}_+^2] \\
& + \frac{3}{4}\sin\theta\sin\theta'\,[(c_{01}^{\mathrm{II}} + c_{0-1}^{\mathrm{II}})\hat{\mathbf{C}}_+^1 + (c_{01}^{\mathrm{II}} - c_{0-1}^{\mathrm{II}})\hat{\mathbf{C}}_-^1 + (s_{0-1}^{\mathrm{II}} - s_{01}^{\mathrm{II}})\hat{\mathbf{S}}_+^1 \\
& + (-s_{01}^{\mathrm{II}} - s_{0-1}^{\mathrm{II}})\hat{\mathbf{S}}_-^1],
\end{aligned}
\tag{46}
$$

with a similar expression for $\hat{\mathbf{M}}_{\mathrm{III}}$, when all c^{II} and s^{II} coefficients (see Eqs. (A1) and (A2)) are replaced by the c^{III} and s^{III} coefficients (see Eqs. (A3) and (A4)), respectively. Various auxiliary coefficients and matrices appearing in Eq. (46) are given in Appendix A. Notice that Eq. (46) has a form similar to Eq. (49) of Stenflo (1998). Also note that the 3/2 factor of Eq. (42) has already been included in the definition of $\hat{\mathbf{M}}_{\mathrm{II}}$ and $\hat{\mathbf{M}}_{\mathrm{III}}$ in Eq. (46). The Hanle-Zeeman PRD grand redistribution matrix is strongly angle dependent, and needs special care in numerical evaluation. This matrix appears inside the scattering integral of the line radiative transfer equation. A sufficiently general form of this matrix is presented in Eq. (43), which takes care of the radiative and collisional contributions in a neatly factorized manner (see Nagendra 1994; Nagendra et al. 1999).

4. A Study of Magnetic Redistribution Functions

The magnetic RF defined in Eqs. (21) – (26) form the basis for the frequency dependence of magnetic redistribution matrices, which are expressed as a combination of different types

of "angular phase matrices" ($\hat{\mathbf{C}}$ and $\hat{\mathbf{S}}$), and the c and s coefficients. A good knowledge about the nature of these basis functions would be useful to understand the physics of Hanle-Zeeman scattering. We will now explore the magnetic RF in some detail. In Sect. 4.1 we discuss the dependence of RF on the scattering angle and incoming frequency for a fixed value of the field strength. The field strength dependence is considered in Sect. 4.2.

4.1. Dependence of the Magnetic RF on Scattering Angle and Incoming Frequency

We will here consider the magnetic RF of Hummer's type II and III for three scattering angles $\Theta = 30°$, $90°$, and $150°$ and incoming frequencies $x' = 0, 2, 4$. The damping parameter is chosen to be $a = 10^{-3}$, and the field strength is chosen such that $v_{\mathrm{H}} = \nu_L/\Delta\nu_{\mathrm{D}} = 1$. We introduce the notion of 'frequency–coherence' ($x \simeq x'$) and 'magnetic–coherence' ($x \simeq v_{\mathrm{H}}$), in order to interpret the results.

4.1.1. RF of type II

The magnetic RF of Hummer's type II are shown in Fig. 2. The solid lines refer to incoming frequency $x' = 0$, the dotted lines to $x' = 2$ and the dashed lines to $x' = 4$. All the thin lines correspond to magnetic quantum number $q = -1$, medium lines to $q = 0$, and thick lines to $q = +1$. The $q = 0$ case represents the non-magnetic scalar RF of Hummer (1962).

The function $R_{\mathrm{II,H}}^q(x, x', \Theta)$ is shown in Fig. 2a. For forward ($\Theta = 0$) scattering, the function $R_{\mathrm{II,H}}^q$ exhibits exact frequency–coherence ($x = x'$) at all the absorption frequencies x', while for backward scattering ($\Theta = \pi$), the function peaks at $x = -x'$ (see e.g. Henyey 1940; Cannon 1985; Wallace & Yelle 1989). This strong coherence is retained for small scattering angles. This can be clearly seen for $\Theta = 30°$. For $|x - qv_{\mathrm{H}}| \leq 3$, the peak position of the RF varies approximately as $x_{\max} = x' \cos\Theta + 2qv_{\mathrm{H}} \sin^2 \Theta/2$ (see also Wallace & Yelle 1989, for the non-magnetic $R_{\mathrm{II,H}}^0$ case). In the non-magnetic $R_{\mathrm{II,H}}^0$ case, it is well known that for arbitrary scattering angles the frequency–coherence behaves in a very unique way, namely with the appearance of a double peak in the transition frequencies ($2 < x' < 4$) — one coherent peak at $x \sim x'$, with the frequency position of the second non-coherent peak depending strongly on scattering angle Θ (see Fig. 7.4 of Cannon 1985). This behavior is also preserved by the RF for $q = \pm 1$. For example, $(q, x') = (-1, 2)$ (thin solid line) and $(+1, 4)$ (thick dashed line) show this double peak profile for both $\Theta = 90°$ and $150°$

scattering angles. Also the RF becomes narrow as the scattering angle changes from 90° to 150° or 30°, which implies a lack of diffusion in frequency space in each scattering event. We note that for the $\Theta = 90°$ case the $(+1, 0)$ (thick solid line) and $(+1, 2)$ (thick dotted line) coincide. Broad coherent emission profiles are observed about $x \sim x'$ for all the components $q = 0, \pm 1$, when (a) the incoming frequencies (x') are large $(x' > 3)$, and (b) the scattering angles are large $(\Theta \geq 90°)$ (cf. the thin, medium, and thick dashed lines for $\Theta = 90°$ and 150° scattering). In addition the $q = +1$ case, as already described, produces double peaks. The $q = +1$ case would show broad peaks about $x \sim x'$, without a non-coherent component, if we chose still larger values for the incoming frequency x'.

In Fig. 2b we show the function $R_{\mathrm{II, F}}^q(x, x', \Theta)$. For $(q, x') = (0, 0)$ (medium solid line), regardless of the scattering angle, $R_{\mathrm{II, F}}^0$ exhibits an emission component similar to the anti-symmetric Faraday-Voigt function. The magnitude of this function increases as we go from $\Theta = 30°$ to 150°. For $\Theta = 30°$ and 90° scattering, the magnetic components $(-1, 0)$ (thin solid lines) are entirely positive and $(+1, 0)$ (thick solid lines) entirely negative. The magnetic components $(\pm 1, 0)$ are highly coherent and nearly symmetric, peaking about $x = 0$ in the $\Theta = 30°$ case. For $\Theta = 90°$ scattering they peak slightly away from line center and are much broader compared to the corresponding small angle scattering case. In the $\Theta = 30°$ case all the components $q = 0, \pm 1$, show highly coherent symmetric peaks at $x = x'$ for both the incoming frequencies $x' = 2$ and 4. Corresponding cases for $\Theta = 90°$ show broad and slightly asymmetric peaks about $x \sim x'$. The profiles corresponding to $\Theta = 150°$ and $x' = 0, 2$ show a complex behavior for scattering via all the magnetic substates $(q = 0, \pm 1)$. All the three magnetic components for $x' = 4$ (dashed lines) show broad emission profiles peaking at about $x \sim 4$. We further note that as the scattering angle decreases, $R_{\mathrm{II, F}}^q$ become increasingly coherent, except for the $(0, 0)$ case, where it is non-coherent.

In type II magnetic RF two competing processes are at work. They are, the frequency–coherent effect (controlled by the Gaussian of Eqs. (21) and (22)), and the magnetic–coherent effect for $R_{\mathrm{II, H}}^q$ (controlled by the Voigt function of Eq. (21)), and sign reversal property for $R_{\mathrm{II, F}}^q$ (controlled by Faraday-Voigt function of Eq. (22)). For small scattering angles $(\Theta \leq 30°)$, it is the frequency–coherent effect that dominates (cf. Fig. 2 – top two panels). As the scattering angle increases, which of these two effects dominate is determined by values of x', q and v_{H} (cf. Fig. 2; see also Fig. 7), taken together.
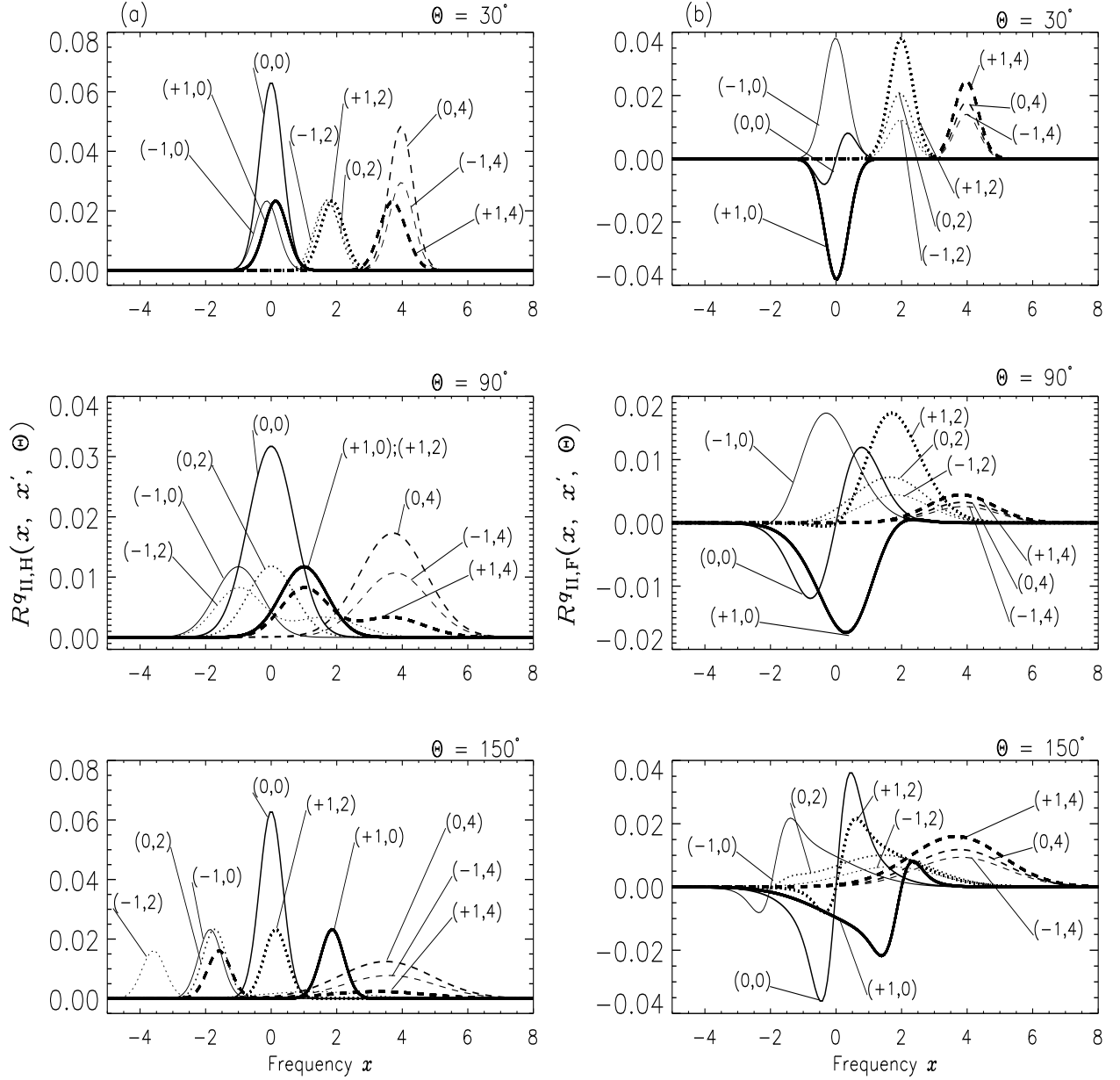
Fig. 2.— The magnetic RF of Hummer's type II. The left panel (Fig. 2a) shows $R^q_{\mathrm{II,\,H}}$, while the right panel (Fig. 2b) shows $R^q_{\mathrm{II,\,F}}$, for different values of the scattering angle. The redistribution function $R^q_{\mathrm{II,\,F}}$ can take negative values. The different line types are labeled with a pair of parameters (q, x'). In all the three panels of Fig. 2a, the thin dotted $(-1, 2)$ and thick dashed $(+1, 4)$ lines are multiplied by 2×10^3, the thin dashed $(-1, 4)$ and medium dashed $(0, 4)$ lines are multiplied by 2×10^4, and the medium dotted $(0, 2)$ line by 20, to be able to present them in the same panel. In Fig. 2b all the dashed lines of the $\Theta = 30°$ case are multiplied by a factor of 2, and of the $\Theta = 150°$ case by 5, in order to show the details clearly. The thin dotted line $(-1, 2)$ and medium dotted line $(0, 2)$ of the $\Theta = 150°$ case in Fig. 2b are multiplied by 2. See Sect. 4.1.1 for discussions.
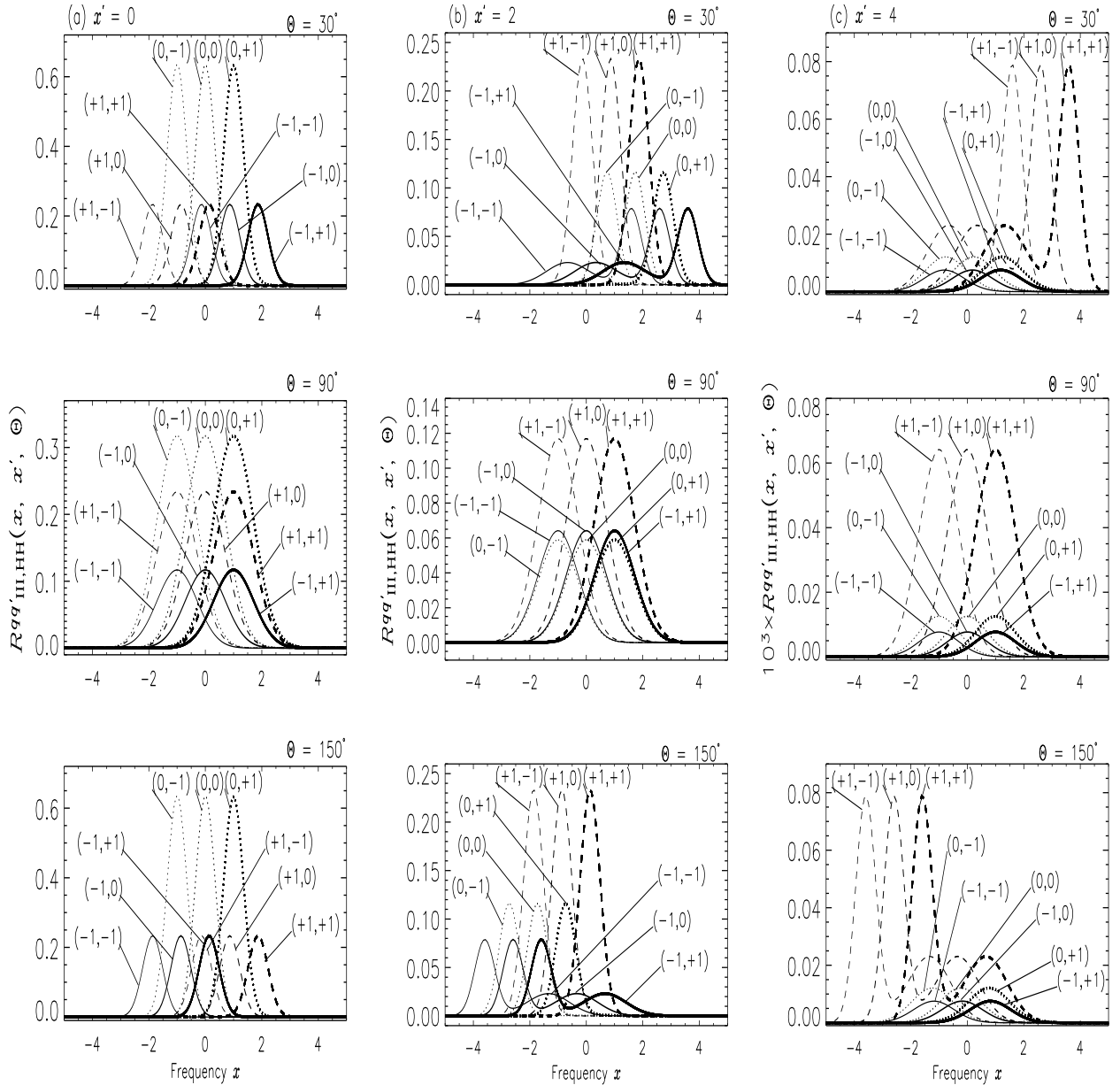
Fig. 3.— Magnetic RF of Hummer's type III. The basis function of type HH is shown. The model parameters are the same as in Fig. 2. In Fig. 3a, in the panel for $\Theta = 90°$, all the dashed lines are multiplied by a factor of 2, since they would otherwise overlap exactly on the solid lines. The different line types are labeled with (q, q') as described in the text. The set of panels exhibit the angular dependence for a given value of x'. The pair (q, q') describes either self-interaction $(q = q')$ or m-state interference $(q \neq q')$. In all three panels of Fig. 3b the solid lines are multiplied by 10^3 and the dotted lines by 10. See Sect. 4.1.2 for discussions.
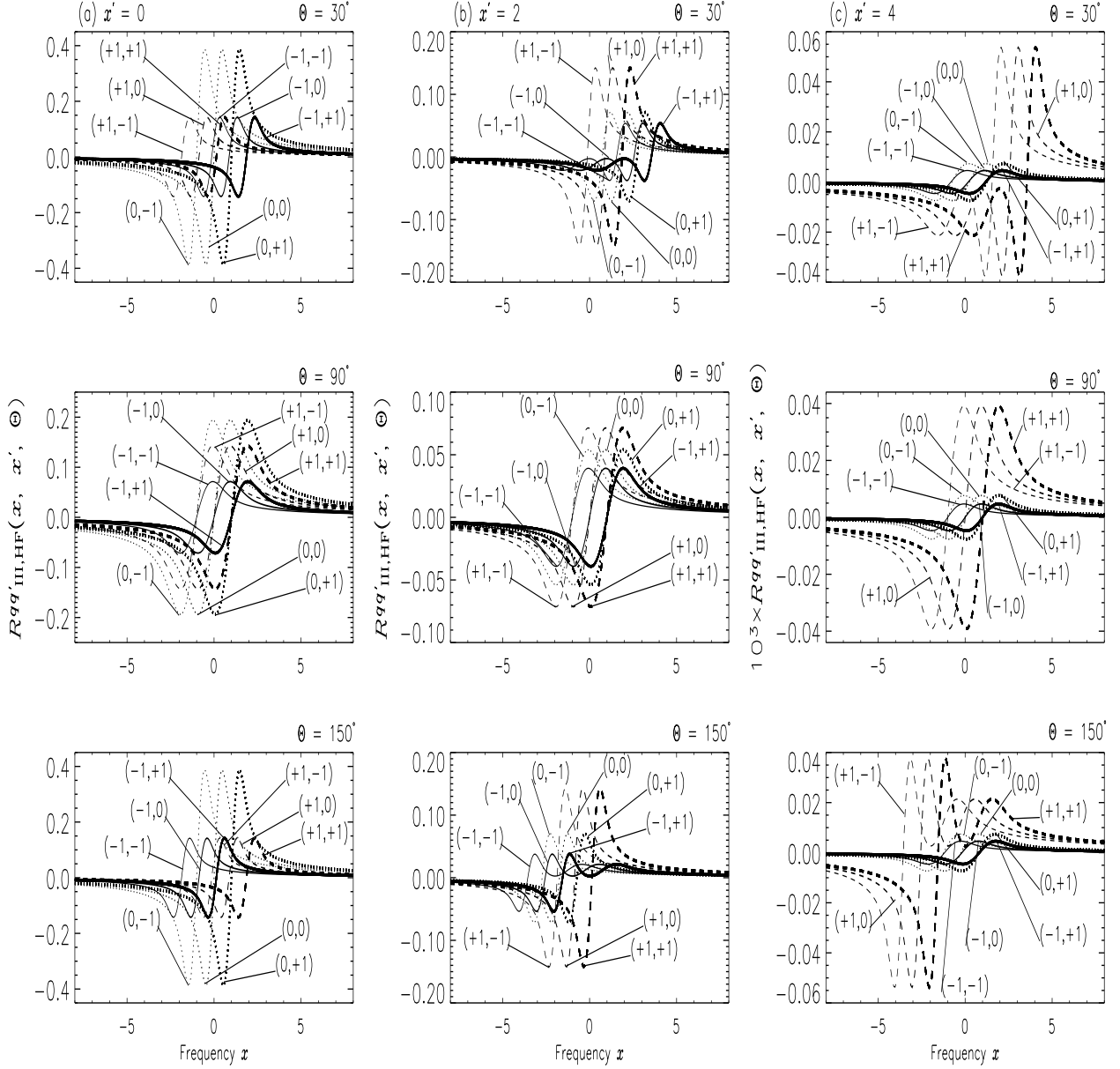
Fig. 4.— Magnetic RF of Hummer's type-III. The basis function of type HF (absorption and dispersion) is shown. This function can have negative values and exhibit the typical behavior of the F function (zero crossing at certain x values, with very slowly decreasing wings for large x). The model parameters are same as in Fig. 3. In Fig. 4b the solid lines in all three panels are multiplied by 10^3, while all the dotted lines for the $\Theta = 30°$ and $150°$ cases are multiplied by 10. See Sect. 4.1.2 for discussions.
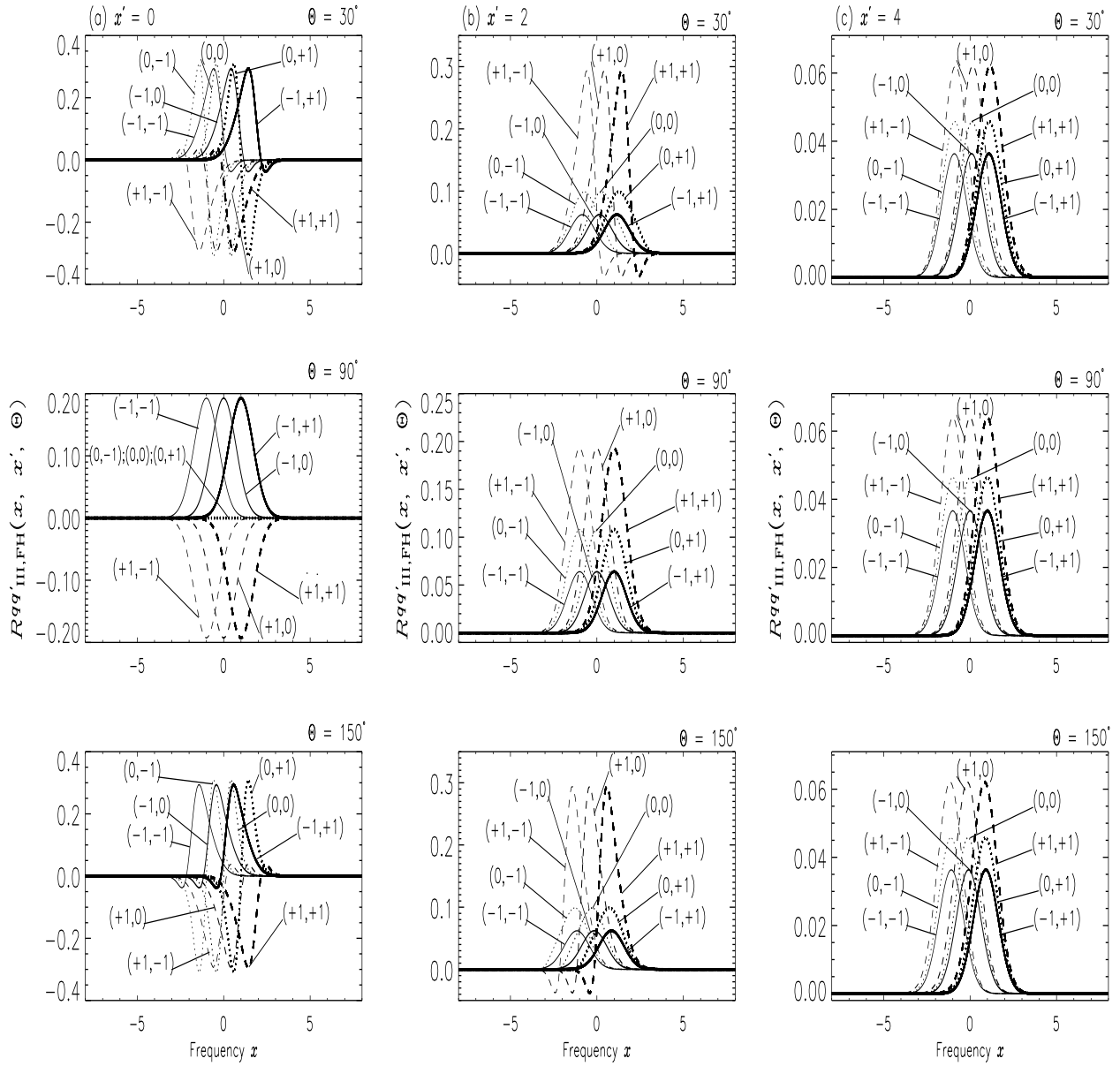
Fig. 5.— Magnetic RF of Hummer's type III. The basis function of type FH is shown. Note that the nature of the FH function is very different from that of HF (displayed in Fig. 4). The function is rather confined to the line core, in contrast to the HF type function, which exhibits very broad wings. The model parameters are same as in Fig. 3. See Sect. 4.1.2 for discussions.
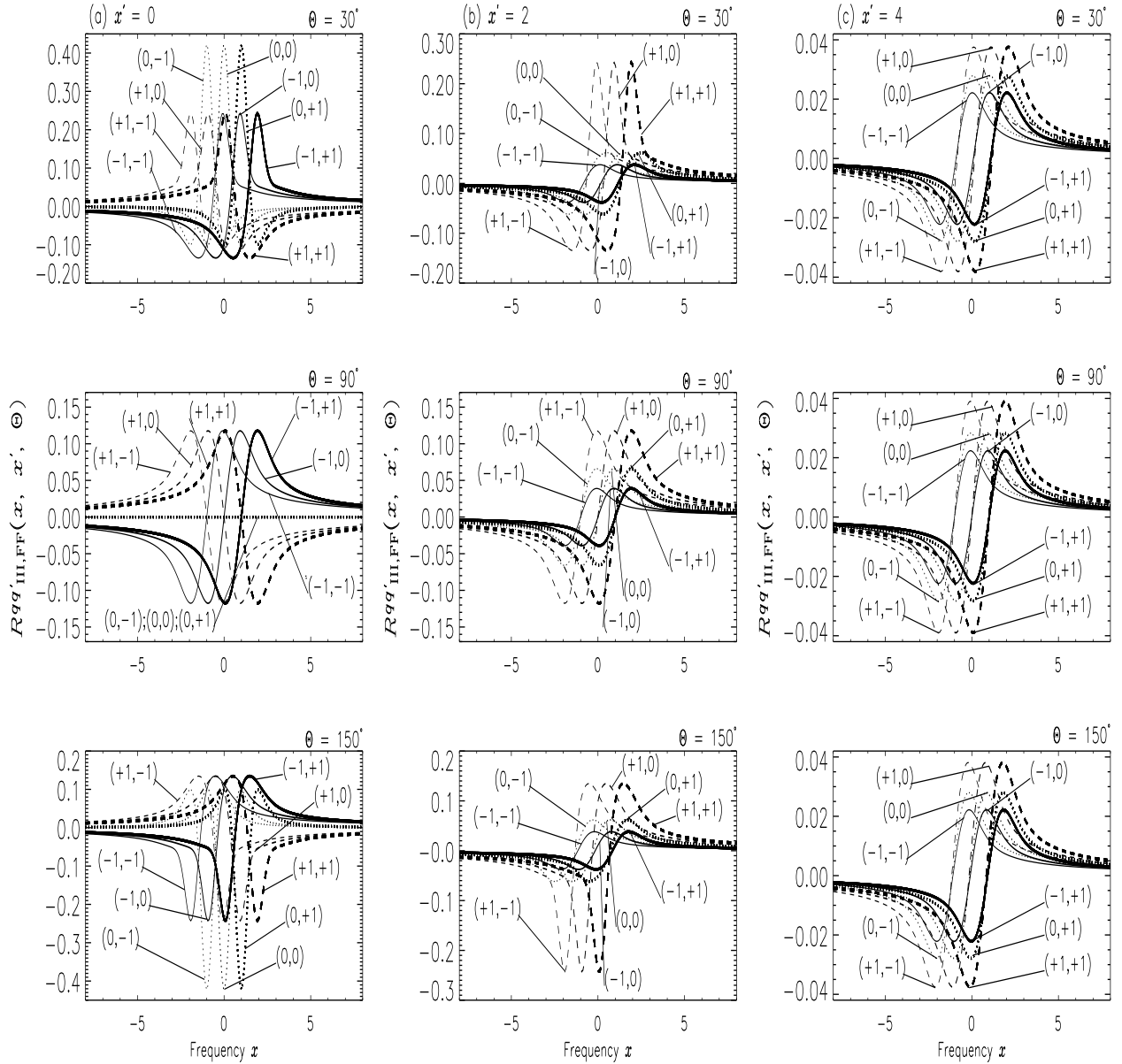
Fig. 6.— Magnetic RF of Hummer's type III. The basis function of type FF is shown. Note the very slow decrease of the function (high level of non-coherence) even in comparison with the HF or FH type functions. The model parameters are the same as in Fig. 3. See Sect. 4.1.2 for details.

4.1.2. RF of type III

The magnetic redistribution functions of Hummer's type III are shown in Figs. 3 - 6, for the same set of parameters as in Fig. 2. Unlike the case of the magnetic RF of Hummer's type II, the type III functions depend on the pair of magnetic quantum numbers (q, q') simultaneously. They in fact refer to the interference between the upper level magnetic sub-states. Thus there are 9 combinations of (q, q'), which are distinguished as different line types of different line thickness. The thin lines refer to the (q, q') pairs as follows: solid: $(-1, -1)$; dotted: $(0, -1)$; dashed: $(+1, -1)$. Medium thickness lines refer as follows: solid: $(-1, 0)$; dotted: $(0, 0)$; dashed: $(+1, 0)$. Thick lines refer as follows: solid: $(-1, +1)$; dotted: $(0, +1)$; dashed: $(+1, +1)$. Note that the HH type profiles with $(q, q') = (0, 0)$ are nothing but the well known Hummer's non-magnetic RF of type III.

Basis Functions of type HH

In Fig. 3 we show $R^{qq'}_{\mathrm{III, HH}}(x, x', \Theta)$ as a function of outgoing frequency x. All profiles shown for the $x' = 4$ case (cf. Fig. 3c) are 3 orders of magnitude smaller than those shown in Fig. 3a. $R^{qq'}_{\mathrm{III, HH}}$ is always positive. Unlike the RF of Hummer's type II, which shows perfect coherence for $\Theta = 0°$, the RF of Hummer's type III is completely non-coherent, CRD like (for $\Theta = 90°$) and does not show coherence even for $\Theta = 0°$. For the $\Theta = 90°$ case, the set of thin $(q, -1)$ and the set of thick $(q, +1)$ line profiles are shifted symmetrically about $x = 0$ and peak at the shifted frequencies $x = \pm 1$. The $(q, 0)$ components (the set of medium lines) are unshifted and peak at $x = 0$. This behavior can be easily understood from Eq. (23), which for $\Theta = 90°$ reduces to

$$R^{qq'}_{\mathrm{III, HH}}(x, x', 90°) = \frac{1}{\pi} H(a, v'_q) H(a, v_{q'}), \tag{47}$$

i.e., it behaves like CRD (complete non-coherence). For $x' = 0$ in particular the functional values of $H(a, v'_{+1} = -1)$ and $H(a, v'_{-1} = +1)$ are the same, because the Voigt function is a symmetric function. As a result the function $R^{qq'}_{\mathrm{III, HH}}(x, x', 90°) = \mathrm{constant} \times H(a, v_{q'})$ for $q = \pm 1$ and $x' = 0$. This implies that all solid lines $(-1, q')$ coincide with the corresponding dashed lines $(+1, q')$. However, to make all the dashed lines visible in Fig. 3a, they have been multiplied by 2. The triplet-like structure centered around $x = 0$ is conserved by the dotted lines $(0, q')$ for $x' = 0$ and all the scattering angles (cf. Fig. 3a). A similar behavior is exhibited by the set of curves for $(+1, q')$ (dashed lines) and $(-1, q')$ (solid lines) magnetic substates also, except that they are centered around frequencies $x = \pm 1$ for $\Theta = 30°$ and $150°$ scattering. For the $x' = 0$ case (cf. Fig. 3a), all the magnetic components of HH type RF show narrow profiles for $\Theta = 30°$ and $150°$ scattering as compared with the $90°$ scattering case.

From Eqs. (23) - (26) one can easily verify that the following reflection symmetry about $x = 0$ is obeyed by the RF :

$$R_{\mathrm{III,\,XH}}^{qq'}(-x,\, x',\, \pi - \Theta) = R_{\mathrm{III,\,XH}}^{q-q'}(x,\, x',\, \Theta), \tag{48}$$

$$R_{\mathrm{III,\,XF}}^{qq'}(-x,\, x',\, \pi - \Theta) = -R_{\mathrm{III,\,XF}}^{q-q'}(x,\, x',\, \Theta), \tag{49}$$

where the symbol X stands for H or F. The above expressions are generalizations of the original non-magnetic symmetry relations described in Cannon (1985) to cover the magnetic scattering case. This reflection symmetry represents a combined symmetry involving both frequencies and angles. In Fig. 3 the panels for $\Theta = 30°$ and $150°$ clearly show this reflection symmetry for $x' = 0,\ 2,\ 4$ and X = H in Eq. (48).

Basis Functions of types HF, FH, *and* FF

Figure 4 shows $R_{\mathrm{III,\,HF}}^{qq'}(x,\, x',\, \Theta)$ as a function of scattering angle Θ ($= 30°,\ 90°,\ 150°$) and scattered frequency x, for three incoming frequencies ($x' = 0,\ 2,\ 4$). $R_{\mathrm{III,\,HF}}^{qq'}$ obviously assumes both positive and negative values. The reflection symmetry of $R_{\mathrm{III,\,HF}}^{qq'}$ given in Eq. (49) with X = H can be clearly seen in Fig. 4 for $\Theta = 30°$ and $150°$. All the magnetic components for the $\Theta = 90°$ scattering case show a similar behavior for $x' = 0,\ 2,\ 4$: all thin lines $(q, -1)$ have a positive peak around $x = 0$ (and a negative peak around $x = -2$); all medium lines $(q, 0)$ peak at $|x| = 1$; all thick lines $(q, +1)$ exhibit a positive peak at $x = 2$ (and a negative peak at $x = 0$). Such a behavior can be understood from Eq. (24), which for $\Theta = 90°$ reduces to

$$R_{\mathrm{III,\,HF}}^{qq'}(x,\, x',\, 90°) = \frac{2}{\pi}\, H(a, v_q')\, F(a, v_{q'}). \tag{50}$$

From Eq. (50) we note that $R_{\mathrm{III,\,HF}}^{qq'}(x,\, x',\, 90°)$ has a zero crossing at $x = q' v_{\mathrm{H}}$, regardless of the value of q (see Fig. 4). In Fig. 4a, the dashed lines for $\Theta = 90°$ have been multiplied by 2, as they would otherwise superimpose on the corresponding solid lines (cf. the discussion following Eq. (47)). The magnetic components $(+1, q')$ (the dashed lines) for $x' = 4$ and $\Theta = 30°$ (and $150°$) show double negative (respectively positive) peaks.

The function $R_{\mathrm{III,\,FH}}^{qq'}(x,\, x',\, \Theta)$ is shown in Fig. 5 for the same set of parameters as in Fig. 4. Like $R_{\mathrm{III,\,HF}}^{qq'}$, the function $R_{\mathrm{III,\,FH}}^{qq'}$ takes both positive and negative values. For $\Theta = 90°$ the nature of all the components of RF can be understood in terms of the Eq. (25), which for this particular case simplifies to

$$R_{\mathrm{III,\,FH}}^{qq'}(x,\, x',\, 90°) = \frac{2}{\pi}\, F(a, v_q')\, H(a, v_{q'}). \tag{51}$$

From Eq. (51) we note that $R_{\text{III, FH}}^{qq'}(x,\, x',\, 90°)$ vanishes when $x' = qv_{\text{H}}$, since then $F(a, v'_q = 0)$ is zero. Thus all dotted lines $(0, q')$ are zero (cf. Fig. 5a). At line center $x' = 0$, the function $F(a, v'_{-1} = 1)$ assumes a positive fixed value, while $F(a, v'_{+1} = -1)$ takes a negative fixed value. Therefore all the solid lines $(-1, q')$ in Fig. 5a are modified Voigt functions $H(a, v_{q'})$, while the dashed lines $(+1, q')$ are modified inverted Voigt functions $-H(a, v_{q'})$. The peak positions of both the solid $(-1, q')$ and dashed $(+1, q')$ lines are given by $x = q'$, since we have chosen $v_{\text{H}} = 1$. The behavior of $R_{\text{III, FH}}^{qq'}(x,\, x',\, 90°)$ for $x' = 2,\, 4$ can also be easily explained in terms of Eq. (51). We note that in Figs. 5b and 5c, the function $R_{\text{III, FH}}^{qq'}(x,\, x',\, 90°)$ is entirely positive, since $F(a, 2-q)$ and $F(a, 4-q)$ are positive for all q. For $x' = -2$ or $x' = -4$, $F(a, -2-q)$ and $F(a, -4-q)$ are negative, which leads to inverted profiles compared to the ones shown in Figs. 5b and 5c for the $\Theta = 90°$ case. The reflection symmetry of $R_{\text{III, FH}}^{qq'}$ as given in Eq. (48) with X = F can be seen in Fig. 5 for $\Theta = 30°$ and 150°. In Fig. 5c for the wing frequency $x' = 4$, the $\Theta = 30°$ and 150° redistribution profiles show behavior similar to that exhibited by $\Theta = 90°$, with a very slight difference in magnitude (angular isotropy of the scattering probability).

The function $R_{\text{III, FF}}^{qq'}(x,\, x',\, \Theta)$ given in Eq. (26) is plotted in Fig. 6. Like the HF, FH type redistribution, $R_{\text{III, FF}}^{qq'}$ also has both positive and negative values. To understand the $\Theta = 90°$ case, we can write Eq. (26) for this particular case as

$$R_{\text{III, FF}}^{qq'}(x,\, x',\, 90°) = \frac{4}{\pi}\, F(a, v'_q)F(a, v_{q'}). \tag{52}$$

From Eq. (52) we note that $R_{\text{III, FF}}^{qq'}(x,\, x',\, 90°)$ vanishes when $x' = qv_{\text{H}}$ (cf. Fig. 6a), like the FH type RF, and has a zero crossing at $x = q'v_{\text{H}}$ (cf. Fig. 6), like the HF type RF. In Fig. 6a for 90° scattering the dotted lines $(0, q')$ are zero, the solid lines $(-1, q')$ are modified Faraday-Voigt functions $F(a, v_{q'})$, while the dashed lines $(+1, q')$ are modified inverted Faraday-Voigt functions $-F(a, v_{q'})$, for the same reason as noted below Eq. (51). The behavior of $R_{\text{III, FF}}^{qq'}(x,\, x',\, 90°)$ for $x' = 2,\, 4$ (cf. Figs. 6b and 6c) can also be easily understood through Eq. (52). The reflection symmetry of $R_{\text{III, FF}}^{qq'}$ as given in Eq. (49) with X = F is clearly seen in Fig. 6 for the scattering angles $\Theta = 30°$ and 150°. Again, when $x' = 4$ and $\Theta = (30°, 150°)$, $R_{\text{III, FF}}^{qq'}$ exhibits a similar behavior as $R_{\text{III, FH}}^{qq'}$ (nearly isotropic angular scattering).

The HF redistribution function is not always similar to the FH type, except for 90° scattering, and in particular, when $q = q'$ (self-interference of m-states). The FH type redistribution is similar to FF for $\Theta = 90°$ scattering, except for the shape of the redistribution function, which for FH resembles a modified Voigt and for FF a modified Faraday-Voigt function. Same arguments hold good for mutual comparison of HH and HF type functions.
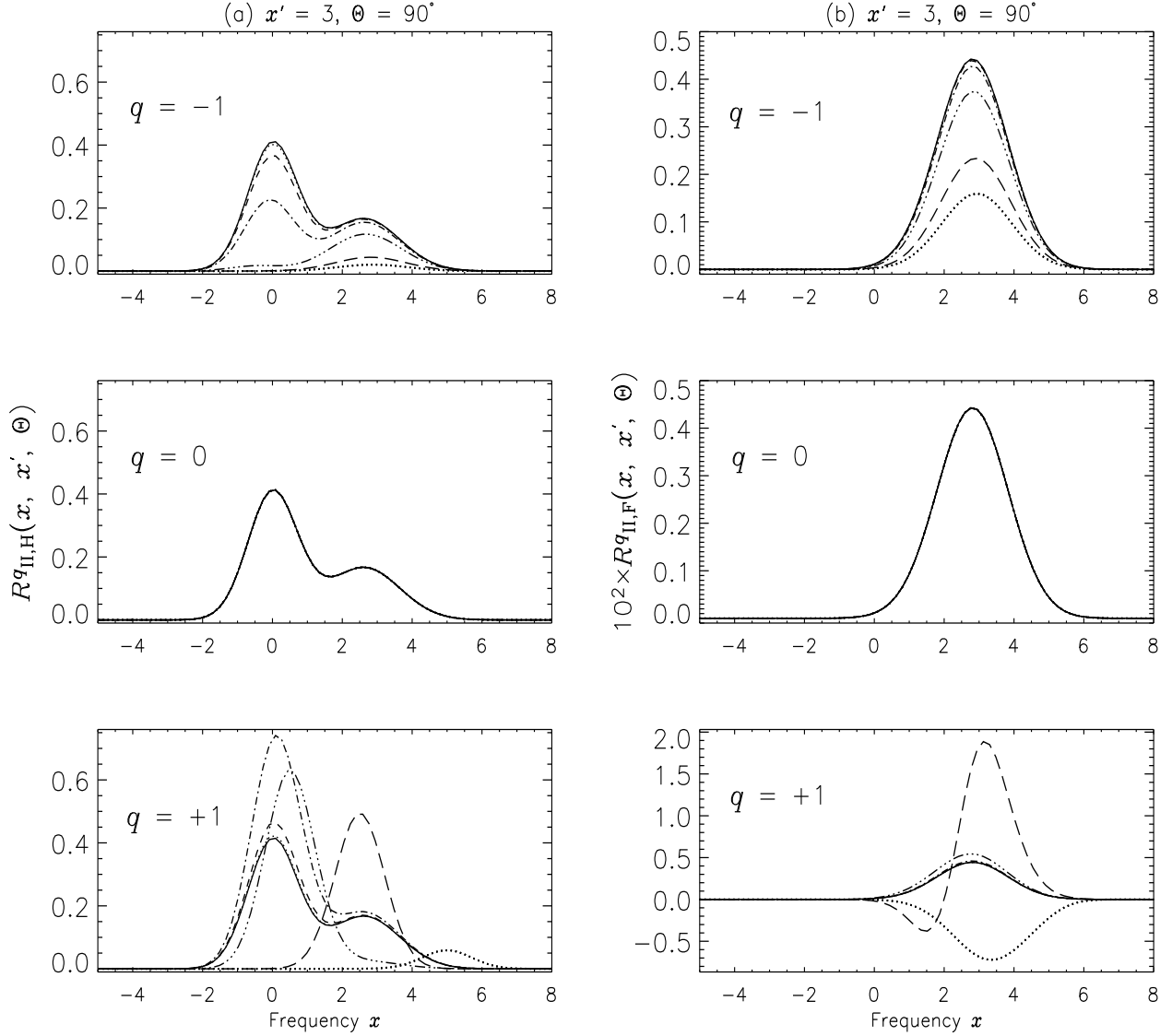
Fig. 7.— Effect of field strength on the Hanle-Zeeman redistribution. The magnetic RF of Hummer's type II is shown. The left panels (Fig. 7a) show $R^q_{\mathrm{II,H}}(x, x', \Theta)$, while the right panels (Fig. 7b) show $R^q_{\mathrm{II,F}}(x, x', \Theta)$, for different values of the field strength, parameterized through v_{H}. The model parameters and line types are given in Sect. 4.2. We note that all curves for $q = -1, 0$ of $R^q_{\mathrm{II,H}}$ (Fig. 7a) are multiplied by a factor of 10^5. For $q = +1$, the solid to the dash-dotted lines (four of the curves) are multiplied by 10^5, the dash-triple dotted line by 10^4, the long-dashed line by 20, and the thick dotted line by 10^2, to be able to have them displayed in the same panel. See Sect. 4.2.1 for discussions.
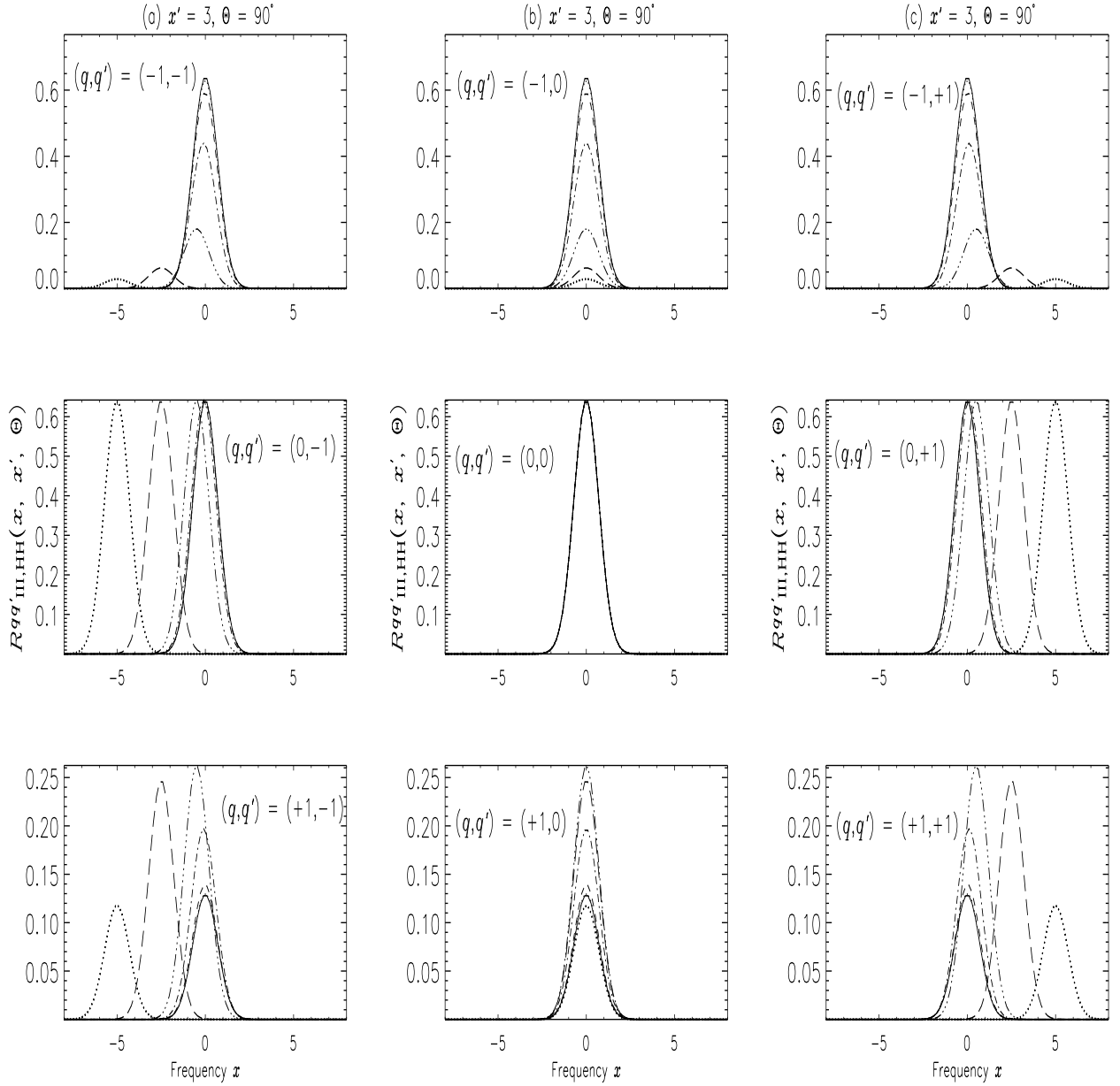
Fig. 8.— Effect of field strength on the magnetic redistribution function $R_{\mathrm{III,HH}}^{qq'}$. The different line types and model parameters are the same as in Fig. 7. All the curves in the two top panels of Figs. 8a-c are multiplied by 10^4. In the bottom panels, the solid to the dash-dotted lines (four curves) are multiplied by 2×10^3, the dash-triple-dotted line by 400, and the thick dotted line by 20. See Sect. 4.2.2 for details.
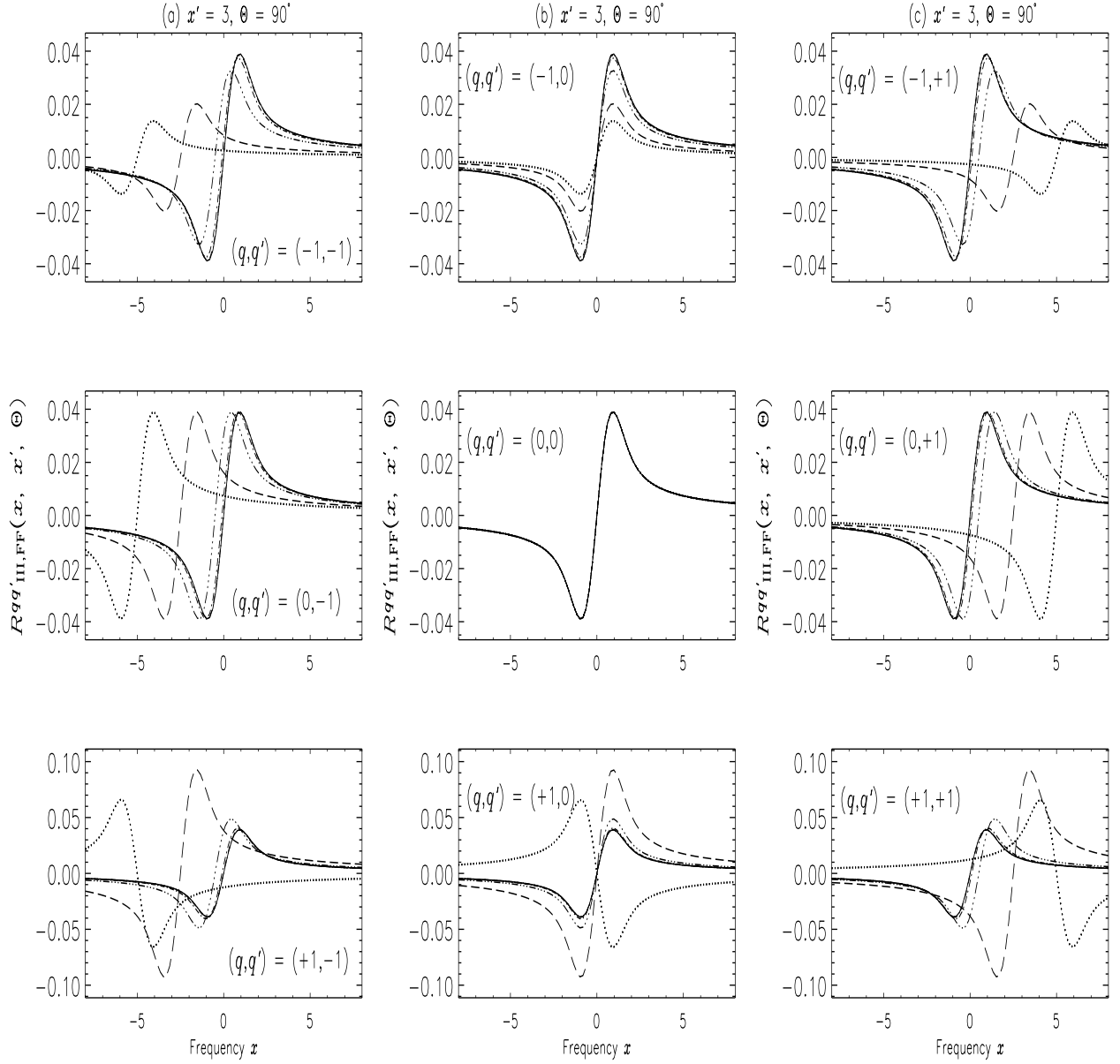
Fig. 9.— Effect of field strength on the magnetic redistribution function $R^{qq'}_{\mathrm{III,\,FF}}$. The different line types and model parameters are the same as in Fig. 7. In all the panels the zero crossing occurs at $x = q'v_{\mathrm{H}}$. See Sect. 4.2.4 for discussions.

4.2. Dependence of the Magnetic RF on Field Strength

To study the dependence of the magnetic RF on v_H (field strength), we chose a scattering geometry that produces maximum linear polarization, namely 90° scattering, assuming a photon with incoming frequency $x' = 3$. The damping parameter is chosen as $a = 10^{-3}$. The field strength parameter v_H is varied as follows: $v_H = 0.0008$ (solid line), 0.004 (dotted line), 0.02 (dashed line), 0.1 (dash-dotted line), 0.5 (dash-triple-dotted line), 2.5 (long-dashed line), and 5 (thick dotted line). This range for v_H covers the weakest fields through intermediate to quite strong fields, with reference to the Doppler width of an optical line (see Stenflo 1998).

4.2.1. Type II RF

Figure 7 shows the $R^q_{II, H}$ and $R^q_{II, F}$ functions of Eqs. (21) and (22). We first discuss $R^q_{II, H}$ (cf. Fig. 7a). The $q = 0$ case is non-magnetic and hence all the curves merge, showing a typical double peaked behavior as discussed with regard to Fig.2a. This double peaked behavior is retained for weak magnetic fields ($v_H \leq 0.1$) for both $q = \pm 1$. The peak amplitudes at $(q, x) = (-1, 0/3)$ diminish as the field strength increases. For $v_H > 0.1$, the $q = -1$ profiles exhibit a single peak at $x \sim x' \sim 3$, which is typical non-magnetic coherence in the case of $R^q_{II, H}$. In contrast the $q = +1$ profiles exhibit magnetic–coherence ($x \simeq v_H$), and the magnitude of $R^q_{II, H}$ increases with increasing v_H, since magnetic–coherence dominates as compared with the $q = -1$ case, for which frequency–coherence dominates. We have found that for small angles ($\Theta \leq 30°$) the highly frequency–coherent behavior of $R^q_{II, H}$ is preserved, even if the field strength is as high as $v_H = 5$. For large angle scattering ($\Theta > 30°$), the peak positions of $R^q_{II, H}$ depend on x', q and v_H as noted in the last paragraph of Sect. 4.1.1. For example, when $x' = 6$ and $v_H = 2.5$, it is the frequency–coherence that dominates and magnetic–coherent peak appears just as a bump (illustration not shown for brevity).

Figure 7b shows $R^q_{II, F}$. For the $q = 0$ case we have a single positive peak at $x \simeq x' \simeq$ 3, as in this case the (non-magnetic) frequency–coherent part (the Gaussian) completely dominates and erases the negative part of Faraday-Voigt function (cf. Eq. (22)). This dominance of frequency–coherence over the dispersive effects remains valid for $q = -1$, but the peak amplitude decreases with increasing v_H. For $q = +1$ this behavior is observed only for weak fields ($v_H \leq 0.5$). For fields with $v_H = 2.5$ the profile shows both positive and negative peaks, as dispersive effects slowly start dominating over the frequency–coherence. For $v_H = 5$ the dispersive effects completely dominate over frequency–coherence effects, resulting in an entirely negative peak at $x \simeq x' \simeq 3$. For $x' = 3$, the $\Theta = 30°$ and $\Theta = 150°$ cases (not illustrated here) largely resemble the $\Theta = 90°$ case, differing only in the magnitude

of $R_{\mathrm{II,F}}^{q}$.

4.2.2. RF of type III, HH

In Fig. 8 we show $R_{\mathrm{III,HH}}^{qq'}(x,\ x'=3,\ \Theta=90°)$ for the same values of the field strength parameter as in Fig. 7. The behavior of $R_{\mathrm{III,HH}}^{qq'}(x,\ 3,\ 90°)$ can be easily understood through Eq. (47). For the case $(q,q')=(q,0)$ the function $R_{\mathrm{III,HH}}^{q0}(x,\ 3,\ 90°)=(1/\pi)H(a,3-qv_{\mathrm{H}})H(a,x)$. Thus the shape of $R_{\mathrm{III,HH}}^{q0}$ is given by $H(a,x)$, irrespective of the value of v_{H}. The effect of v_{H} is only to scale $H(a,x)$ up or down, as can be seen from Fig. 8b, where the peak amplitude decreases with increasing v_{H} for $q=-1$, while for $q=+1$ the peak amplitude increases with v_{H}, reaching a maximum for $v_{\mathrm{H}}=2.5$ (since then $H(a,3-qv_{\mathrm{H}})$ becomes $H(a,0.5)$), and then decreases for $v_{\mathrm{H}}>2.5$. In other words, for the $(q,q')=(+1,0)$ case the largest peak amplitude corresponds to the case when $x'=v_{\mathrm{H}}$.

For the case $(-1,q')$ (the top panels of Figs. 8a-c) the function $R_{\mathrm{III,HH}}^{-1q'}(x,\ 3,\ 90°)=(1/\pi)H(a,3+v_{\mathrm{H}})H(a,x-q'v_{\mathrm{H}})$. Thus $R_{\mathrm{III,HH}}^{-1q'}$ peaks at $x=q'v_{\mathrm{H}}$. However, as v_{H} increases, the peak amplitude decreases, since the scaling factor $H(a,3+v_{\mathrm{H}})$ decreases with v_{H}. In the case of $(0,q')$ (the middle panels of Figs. 8a-c) the function $R_{\mathrm{III,HH}}^{0q'}(x,\ 3,\ 90°)=(1/\pi)H(a,3)H(a,x-q'v_{\mathrm{H}})$. Again the peak position is governed by $H(a,x-q'v_{\mathrm{H}})$, but now the scaling factor is independent of v_{H}. Therefore the peak amplitude of the $q'=-1$ and $q'=+1$ curves and the different v_{H} curves are identical. In the case of $(+1,q')$ (the bottom panels of Figs. 8a-c) the function $R_{\mathrm{III,HH}}^{+1q'}(x,\ 3,\ 90°)=(1/\pi)H(a,3-v_{\mathrm{H}})H(a,x-q'v_{\mathrm{H}})$. The shape and peak position are governed by $H(a,x-q'v_{\mathrm{H}})$, while the scaling factor increases until $v_{\mathrm{H}}=3$ and then decreases for $v_{\mathrm{H}}>3$.

For scattering angles $\Theta=30°$ and $\Theta=150°$ (not illustrated here), $R_{\mathrm{III,HH}}^{qq'}$ shows basically the similar type of behavior as for $\Theta=90°$, except that the shape of $R_{\mathrm{III,HH}}^{00}$ is rather similar to $(-1,0)$ (medium solid line in Fig. 3b), and the peak positions and shapes of the other components are now determined not only by v_{H} but also by the scattering angle Θ.

4.2.3. RF of type III, HF

The function $R_{\mathrm{III,HF}}^{qq'}(x,\ x',\ 90°)$ is given by Eq. (50). Clearly the dependence of $R_{\mathrm{III,HF}}^{qq'}$ on v_{H} will be the same as that of $R_{\mathrm{III,HH}}^{qq'}$, except that the shape of $R_{\mathrm{III,HF}}^{qq'}$ is now determined by the dispersion profile $F(a,x-q'v_{\mathrm{H}})$ instead of the absorption profile $H(a,x-q'v_{\mathrm{H}})$. Therefore we do not present these profiles here.

4.2.4. RF of type III, FF

The redistribution functions $R_{\text{III, FF}}^{qq'}(x, x' = 3, \Theta = 90°)$ for the same range of the field strength parameter v_{H} as in Figs. 7 and 8 are shown in Fig. 9. The form of the FF type RF for $\Theta = 90°$ is given in Eq. (52). Clearly the shape and peak position are determined by the function $F(a, x - q'v_{\text{H}})$. For $q' = 0$ it follows from Eq. (52) that $R_{\text{III, FF}}^{q0}(x, 3, 90°) = (4/\pi)F(a, 3 - qv_{\text{H}})F(a, x)$. Hence the shape is basically governed by $F(a, x)$, which is scaled up or down by $F(a, 3 - qv_{\text{H}})$. For $q = -1$ the scaling factor $F(a, 3 + v_{\text{H}})$ is positive and decreases as v_{H} increases. Therefore the peak amplitude of $R_{\text{III, FF}}^{-10}$ decreases with increasing v_{H}. In contrast, for $q = +1$, the scaling factor $F(a, 3 - v_{\text{H}})$ is positive as long as $v_{\text{H}} < 3$ and becomes negative for $v_{\text{H}} > 3$. Thus, as clearly shown in Fig. 9, $R_{\text{III, FF}}^{+10}$ reverses sign for $v_{\text{H}} = 5$. Further, since $F(a, 3 - v_{\text{H}})$ increases with v_{H} until $v_{\text{H}} < 3$ and then starts decreasing for $v_{\text{H}} > 3$, the function $R_{\text{III, FF}}^{+10}$ also exhibits the same behavior.

The zero crossing of $R_{\text{III, FF}}^{qq'}(x, 3, 90°)$ is at $x = q'v_{\text{H}}$, as noted below Eq. (52). When $(q, q')=(-1, q')$ (the top panels of Figs. 9a-c) we have $R_{\text{III, FF}}^{-1q'}(x, 3, 90°) = (4/\pi)F(a, 3 + v_{\text{H}})F(a, x - q'v_{\text{H}})$. As already noted, $F(a, 3 + v_{\text{H}})$ decreases with v_{H} and hence $R_{\text{III, FF}}^{-1q'}$ also decreases with v_{H}. For $(0, q')$ the scaling factor is independent of v_{H} (as it equals $F(a, 3)$). Thus all the curves in the middle panels of Figs. 9a-c have the same value for their peak amplitude. For $(+1, q')$ the same behavior as noted for $(+1,0)$ is observed (see bottom panels of Figs. 9a-c).

The above discussion on the dependence of $R_{\text{III, FF}}^{qq'}$ on v_{H} is also qualitatively valid for scattering angles other than $\Theta = 90°$.

4.2.5. RF of type III, FH

The dependence of $R_{\text{III, FH}}^{qq'}$ on field strength for 90° scattering is basically the same as that discussed for $R_{\text{III, FF}}^{qq'}$, the only difference being the shape and peak position of $R_{\text{III, FH}}^{qq'}$, which are determined by $H(a, x - q'v_{\text{H}})$ (cf. Eq. (51)). Hence we do not illustrate these functions here.

5.   Extension to the General Quantum Scattering Case

Our treatment so far has been limited to the special case of a $J = 0 \rightarrow 1 \rightarrow 0$ scattering transition, since this case can be dealt with in terms of classical time-dependent oscillator theory and is sufficiently simple to allow a comprehensive and explicit analytical treatment

of the full and general polarized redistribution problem in the presence of arbitrary magnetic fields. With this foundation we can now address the issue of how to extend our polarized PRD theory for the restricted case of triplet to more general case of atomic and molecular transitions involving arbitrary quantum numbers. Here we indicate how such an extension is possible and conceptually already understood, although it is outside the scope of this paper to present this extension in explicit form.

The extension proceeds in a phenomenological way, on the direct analogy between the Kramers-Heisenberg scattering amplitude in quantum mechanics and the Jones matrix for classical scattering. The Jones scattering matrix for the classical case can be written (see Eq. (8.116) of Stenflo 1994) as

$$w_{\alpha\beta} \sim \sum_q \Phi_{-q} \, \varepsilon_q^{\alpha*} \, \varepsilon_q^{\beta} \,, \tag{53}$$

while the Kramers-Heisenberg version for general combinations of quantum numbers (see Eq. (1) in Stenflo 1998) is

$$w_{\alpha\beta} \sim \sum_b \frac{\langle f|\hat{r} \cdot e_\alpha|b\rangle \langle b|\hat{r} \cdot e_\beta|a\rangle}{\omega_{bf} - \omega - i\gamma/2}. \tag{54}$$

a represents the set of quantum numbers (including the magnetic substates) for the initial state, b the corresponding set for the intermediate state, and f for the final state. ω_{bf} is the resonant frequency for a transition between the magnetic substates with upper magnetic quantum number m_b and lower magnetic quantum number m_f. Eq. (54) may be rewritten as

$$w_{\alpha\beta} \sim \sum_b t_{ab} \, t_{bf} \, \Phi_{-q} \, \varepsilon_q^{\alpha*} \, \varepsilon_{q'}^{\beta} \,. \tag{55}$$

Here

$$q = m_f - m_b \quad q' = m_a - m_b \,. \tag{56}$$

t_{ab} and t_{bf} are respectively the two transition amplitudes (including sign) for the transitions between the intermediate state b and the initial and final states a and f, given by the matrix elements in Eq. (54). Φ_{-q} is the normalized profile function that has the same form as the one in Eq. (54) with ω_{bf} given by $(\omega_0 - q\omega_L)$ in the classical case. In the quantum case $-q\,\omega_L$ is replaced by $(g_b m_b - g_f m_f)\omega_L$, where ω_L is the Larmor frequency and $g_{b,f}$ are the Landé factors of the intermediate and final states.

When comparing the classical Eq. (53) with the quantum Eq. (55) we see that they are the same, with two differences: (1) The transition amplitudes t between the magnetic substates involved in the scattering transition appear as weights. They are not needed in

the classical or $J = 0 \to 1 \to 0$ case, since in this case the three amplitudes involved are identical. (2) In one of the geometric ε factors a q' appears instead of a q.

These two differences between the classical and quantum case however do not influence the frequency redistribution for an individual m state scattering transition. The product of the transition amplitudes provides a global, frequency-independent scaling factor for the strength of the scattering transition. The frequency-independent ε factors represent pure geometric projections, and also have nothing to do with the frequency redistribution problem. All the frequency redistribution physics is contained in the only frequency dependent factor, namely Φ_{-q}, the profile function, which is the same in the classical and quantum case.

Now it needs to be remembered that the profile function given in the usual version (Eq. (54)) of the Kramers-Heisenberg dispersion formula, refers to the atomic frame without Doppler motions or collisions. This is the frequency–coherent case. The whole problem of frequency redistribution arises exclusively due to the presence of collisions in the atomic frame, and in addition due to Doppler shifts in the observer's frame, and to the circumstance that the Doppler and collisional redistributions get coupled in an intricate way. Once we have specified the collisional redistribution in the atomic frame, the transformation to the observer's frame, while being mathematically complicated, merely involves the introduction of Doppler redistribution, which has nothing to do with the question of whether the atomic-frame redistribution has been treated with quantum or classical physics.

The whole question of redistribution therefore boils down to the question on how to treat the collisional redistribution in the general quantum mechanical case. The way that we did it in the classical case was to solve the time-dependent equation for an oscillating electron. When the oscillator equation was decomposed in complex spherical vectors, it decoupled into independent component equations, one for each q. The solution could then be expressed with two terms, one for the static and one for the transitory solution in the atomic frame. The frequency–coherent part R_{II} of the redistribution has its source in the stationary solution, while the complete redistribution part R_{III} has its source in the transitory solution.

In the classical collision theory of Stenflo (1994) and BS99 the effect of elastic collisions is to destroy the phase coherence by truncating the damped oscillation of the transitory solution (the stationary solution is not affected by the collisions, since it is driven by the incident electromagnetic field). This leads to both collisional broadening and to collisional depolarization ($D^{(K)}$), with a depolarization rate that is half the broadening rate (γ_c).

An immediate and natural phenomenological extension of the classical collision theory to general quantum transitions is to treat each radiative emission transition between magnetic substates m_b and m_f, which represents a given value of q in the quantum Eq. (55), as a

damped oscillation that gets truncated by collisions. The subsequent Fourier transformation of this truncated oscillation then leads to the broadening and depolarization in exactly the same way as in the classical case. Therefore, when considering the scattering transitions for each individual combination of m states separately, the classical frequency redistribution theory can be carried over to be used directly.

In this way we have fully defined how the present theory can be generalized to any quantum scattering transitions. Although the classical and quantum cases behave the same for transitions between the individual m states, the two cases will differ considerably when the individual m state transitions are added together due to the different transition strengths and due to the different $m_a \rightarrow m_f$ combinations in the geometric factors. These differences will be enhanced and convolved when the bilinear products between the Jones matrix elements are formed (see Eq. (8) of Stenflo 1998), which contain the various interference terms that describe the Hanle effect.

A further extension can be done to the case when the ground state acquires atomic polarization due to optical pumping. This is done by attaching the weight $\rho_{m_a m_{a'}}$ to the bilinear products $w_{\alpha\beta}\, w^*_{\alpha'\beta'}$ before summing over all the initial m states m_a and $m_{a'}$. Here $\rho_{m_a m_{a'}}$ is a density matrix element of the initial state. When m_a equals $m_{a'}$, then ρ describes the m state population, when they are different it describes the m state coherences. ρ has to be found by solving the statistical equilibrium problem.

Although a full generalization of our polarized redistribution theory for arbitrary magnetic fields is thus rather straightforward, it does not easily lend itself to a comprehensive presentation in such an explicit analytical form, as we could do here for the special $J = 0 \rightarrow 1 \rightarrow 0$ case. The various magnetic redistribution basis functions with their intrinsic symmetries that we have described for the special case, continue to be ingredients in any general quantum redistribution theory, although these basis functions will be combined and weighted differently from case to case, depending on the particular combination of quantum numbers. Nevertheless, the present work provides insight into the mathematical structure of the general case while elucidating the underlying physics.

6. Concluding Remarks

The discovery of the wealth of structures in the Second Solar Spectrum has created an urgent need for new theoretical tools, which were not available before, since there had not been a concrete demand for them. Still the theory is severely lagging behind the observational developments. The full Second Solar Spectrum has been mapped with high spectral reso-

lution and polarimetric sensitivity from 3100 – 7000 Å. The spatial and temporal variations of the scattering polarization in selected portions of the Second Solar Spectrum are being explored in various magnetic regions on the Sun, and narrow-band filter systems are being introduced to map the Hanle-Zeeman effect in different spectral lines (Feller et al. 2006). Many of these lines are strong chromospheric lines with both Doppler core and damping wings, and they offer great promise for diagnosing the magnetic field in the solar chromosphere via the Hanle effect. This promise can only be fulfilled if we have the right tools for a quantitative analysis of the observations. For chromospheric lines these tools need to account for partial frequency redistribution (PRD) of polarized radiation in the presence of magnetic fields of arbitrary strength and orientation. In the present paper we have developed this theory in the form of the Hanle-Zeeman redistribution matrix, and we have explored its mathematical structure in detail.

Our PRD theory is based on a classical approach, via the solution of the time-dependent classical oscillator equation. This might seem as a limited approach, and that a correct treatment should instead be in terms of quantum physics. However, as we will show explicitly in a forthcoming paper, our classical approach produces a Hanle-Zeeman redistribution matrix that is identical to that obtained with a perturbative quantum field theory for a $J = 0 \rightarrow 1 \rightarrow 0$ scattering transition. All the mathematical functions that we have described in the present paper, including all their intricate relations and symmetries, are obtained exactly via QED. This equivalence is far from obvious and instead rather miraculous, hinting at a deeper meaning, since the formalisms are vastly different, and the quantum theory is perturbative while the classical theory is non-perturbative. Here we have used the classical approach, since it is (in our opinion) much more transparent and lends itself to a more intuitive understanding of the physics involved.

Several chromospheric spectral lines are of the type $J = 0 \rightarrow 1 \rightarrow 0$ that we have treated here. Examples are the well-studied Ca I 4227 Å line and the Cr I 3594 Å line, which is found (for still unknown reasons) to be the most polarizing line in the whole spectrum (from 3100 – 7000 Å) (Stenflo 2006). Most other lines have different quantum number structures, which means that the present PRD theory needs to be extended to cover these other cases. In the preceding section we have outlined how a straightforward extension can be done, and how the mathematical framework of the present paper can be used as an ingredient of such a generalized theory. Since the theory can be discussed in a comprehensive way for the special $J = 0 \rightarrow 1 \rightarrow 0$ case, we have limited our explicit treatment to this particular case, while showing how it may be generalized.

While we now have a well formulated and understood theory for the general Hanle-Zeeman redistribution matrix, its practical implementation within a polarized radiative-

transfer framework will be a major challenge, in particular the development of numerical computer codes that can solve the polarized transfer problem with PRD for realistic magnetized atmospheres. The present paper lays a foundation for progress toward this goal.

A. The Auxiliary coefficients and phase matrices related to the redistribution matrix $\hat{\mathbf{R}}(x, \mathbf{n}; x', \mathbf{n}')$

Here we list the various auxiliary coefficients and matrices appearing in Eq. (46) in the text. Following Stenflo (1998) we introduce the auxiliary coefficients:

$$
\begin{aligned}
c_{qq'}^{\mathrm{II}} &= \cos\beta_{q-q'}\left\{\cos[(q-q')(\phi-\phi')]\left(h_{qq'}^{\mathrm{II}}\cos\beta_{q-q'} - f_{qq'}^{\mathrm{II}}\sin\beta_{q-q'}\right)\right.\\
&\quad \left. + \sin[(q-q')(\phi-\phi')]\left(h_{qq'}^{\mathrm{II}}\sin\beta_{q-q'} + f_{qq'}^{\mathrm{II}}\cos\beta_{q-q'}\right)\right\},
\end{aligned} \tag{A1}
$$

$$
\begin{aligned}
s_{qq'}^{\mathrm{II}} &= \cos\beta_{q-q'}\left\{\sin[(q-q')(\phi-\phi')]\left(h_{qq'}^{\mathrm{II}}\cos\beta_{q-q'} - f_{qq'}^{\mathrm{II}}\sin\beta_{q-q'}\right)\right.\\
&\quad \left. - \cos[(q-q')(\phi-\phi')]\left(h_{qq'}^{\mathrm{II}}\sin\beta_{q-q'} + f_{qq'}^{\mathrm{II}}\cos\beta_{q-q'}\right)\right\},
\end{aligned} \tag{A2}
$$

for type II functions, and

$$
\begin{aligned}
c_{qq'}^{\mathrm{III}} &= \cos\beta_{q-q'}\cos\alpha_{q-q'}\left\{\cos[(q-q')(\phi-\phi')]\left[(\Re[h_{qq'}^{\mathrm{III}}] - \Im[f_{qq'}^{\mathrm{III}}])\cos(\beta_{q-q'}+\alpha_{q-q'})\right.\right.\\
&\quad \left. - (\Im[h_{qq'}^{\mathrm{III}}] + \Re[f_{qq'}^{\mathrm{III}}])\sin(\beta_{q-q'}+\alpha_{q-q'})\right] + \sin[(q-q')(\phi-\phi')]\left[(\Im[h_{qq'}^{\mathrm{III}}]\right.\\
&\quad \left.\left. + \Re[f_{qq'}^{\mathrm{III}}])\cos(\beta_{q-q'}+\alpha_{q-q'}) + (\Re[h_{qq'}^{\mathrm{III}}] - \Im[f_{qq'}^{\mathrm{III}}])\sin(\beta_{q-q'}+\alpha_{q-q'})\right]\right\},
\end{aligned} \tag{A3}
$$

$$
\begin{aligned}
s_{qq'}^{\mathrm{III}} &= \cos\beta_{q-q'}\cos\alpha_{q-q'}\left\{\sin[(q-q')(\phi-\phi')]\left[(\Re[h_{qq'}^{\mathrm{III}}] - \Im[f_{qq'}^{\mathrm{III}}])\cos(\beta_{q-q'}+\alpha_{q-q'})\right.\right.\\
&\quad \left. - (\Im[h_{qq'}^{\mathrm{III}}] + \Re[f_{qq'}^{\mathrm{III}}])\sin(\beta_{q-q'}+\alpha_{q-q'})\right] - \cos[(q-q')(\phi-\phi')]\left[(\Im[h_{qq'}^{\mathrm{III}}]\right.\\
&\quad \left.\left. + \Re[f_{qq'}^{\mathrm{III}}])\cos(\beta_{q-q'}+\alpha_{q-q'}) + (\Re[h_{qq'}^{\mathrm{III}}] - \Im[f_{qq'}^{\mathrm{III}}])\sin(\beta_{q-q'}+\alpha_{q-q'})\right]\right\},
\end{aligned} \tag{A4}
$$

for type III functions. The angular phase matrices appearing in Eq. (46) are listed below:

$$
\hat{\mathbf{C}}_0^0 = (1-\mu^2)(1-\mu'^2)\begin{bmatrix} 1 & 1 & 0 & 0 \\ 1 & 1 & 0 & 0 \\ 0 & 0 & 0 & 0 \\ 0 & 0 & 0 & 0 \end{bmatrix}, \tag{A5}
$$

$$\hat{\mathbf{C}}_+^0 = \frac{1}{2} \begin{bmatrix} (1+\mu^2)(1+\mu'^2) & -(1+\mu^2)(1-\mu'^2) & 0 & 0 \\ -(1-\mu^2)(1+\mu'^2) & (1-\mu^2)(1-\mu'^2) & 0 & 0 \\ 0 & 0 & 0 & 0 \\ 0 & 0 & 0 & 4\mu\mu' \end{bmatrix},$$

(A6)

$$\hat{\mathbf{C}}_-^0 = \begin{bmatrix} 0 & 0 & 0 & (1+\mu^2)\mu' \\ 0 & 0 & 0 & -(1-\mu^2)\mu' \\ 0 & 0 & 0 & 0 \\ \mu(1+\mu'^2) & -\mu(1-\mu'^2) & 0 & 0 \end{bmatrix},$$

(A7)

$$\hat{\mathbf{C}}_+^2 = \frac{1}{2} \begin{bmatrix} (1-\mu^2)(1-\mu'^2) & -(1-\mu^2)(1+\mu'^2) & 0 & 0 \\ -(1+\mu^2)(1-\mu'^2) & (1+\mu^2)(1+\mu'^2) & 0 & 0 \\ 0 & 0 & 4\mu\mu' & 0 \\ 0 & 0 & 0 & 0 \end{bmatrix},$$

(A8)

$$\hat{\mathbf{S}}_+^2 = \begin{bmatrix} 0 & 0 & -(1-\mu^2)\mu' & 0 \\ 0 & 0 & (1+\mu^2)\mu' & 0 \\ \mu(1-\mu'^2) & -\mu(1+\mu'^2) & 0 & 0 \\ 0 & 0 & 0 & 0 \end{bmatrix},$$

(A9)

$$\hat{\mathbf{C}}_+^1 = \mu\mu' \begin{bmatrix} 1 & 1 & 0 & 0 \\ 1 & 1 & 0 & 0 \\ 0 & 0 & 0 & 0 \\ 0 & 0 & 0 & 0 \end{bmatrix} + \hat{\mathbf{E}}_{33} + \hat{\mathbf{E}}_{44} ; \qquad \hat{\mathbf{C}}_-^1 = \begin{bmatrix} 0 & 0 & 0 & \mu \\ 0 & 0 & 0 & \mu \\ 0 & 0 & 0 & 0 \\ \mu' & \mu' & 0 & 0 \end{bmatrix},$$

(A10)

$$\hat{\mathbf{S}}_+^1 = \begin{bmatrix} 0 & 0 & \mu & 0 \\ 0 & 0 & \mu & 0 \\ -\mu' & -\mu' & 0 & 0 \\ 0 & 0 & 0 & 0 \end{bmatrix} ; \qquad \hat{\mathbf{S}}_-^1 = \hat{\mathbf{E}}_{43} - \hat{\mathbf{E}}_{34}.$$

(A11)

Here $\hat{\mathbf{E}}_{ij}$ denotes a matrix that has a single element $E_{ij} = 1$, while all the remaining elements are zero. We note that the above matrices are identical to those introduced in Stenflo (1998).

REFERENCES

Bommier, V. 1997a, A&A, 328, 706

Bommier, V. 1997b, A&A, 328, 726

Bommier, V. 1999, in Proc. of 2nd SPW, ASSl 243, Solar Polarization, ed. K. N. Nagendra, & J. O. Stenflo (Kluwer Academic Publishers), 45

Bommier, V., & Stenflo, J. O. 1999, A&A, 350, 327 [BS99]

Bommier, V. 2003, in Proc. of 3rd SPW, ASP Conf. Ser. 307, Solar Polarization, ed. J. Trujillo Bueno, & J. Sánchez Almeida (Astronomical Society of the Pacific), 317

Cannon, C. J. 1985, The Transfer of Spectral Line Radiation (Cambridge: Cambridge University Press)

Cooper, J., Ballagh, R. J., Burnett, K., & Hummer, D. G. 1982, ApJ, 260, 299

Casini, R., & Manso Sainz, R. 2005, ApJ, 624, 1025

Domke, H., & Hubeny, I. 1988, ApJ, 384, 527

Faurobert-Scholl, M. 1992, A&A, 258, 521

Feller, A., Boller, A., & Stenflo, J. O. 2006, in Proc. 4th SPW, ASP Conf. Ser., Solar Polarization, ed. R. Casini, & B. W. Lites (Astronomical Society of the Pacific), in press

Fluri, D. M., Holzreuter, R., Klement, J., & Stenflo, J. O. 2003a, in Proc. of 3rd SPW, ASP Conf. Ser. 307, Solar Polarization, ed. J. Trujillo Bueno, & J. Sánchez Almeida (Astronomical Society of the Pacific), 263

Fluri, D. M., Nagendra, K. N., & Frisch, H. 2003b, A&A, 400, 303

Gandorfer, A. 2000, The Second Solar Spectrum, Vol I : 4625 Å to 6995 Å line (Zurich : VdF), ISBN No. 3 7281 2764 7

Gandorfer, A. 2002, The Second Solar Spectrum, Vol II : 3910 Å to 4630 Å line (Zurich : VdF), ISBN No. 3 7281 2844 4

Gandorfer, A. 2005, The Second Solar Spectrum, Vol III : 3160 Å to 3915 Å line (Zurich : VdF), ISBN No. 3 7281 3018 4

Heinzel, P. 1981, J. Quant. Spec. Radiat. Transf., 25, 483

Henyey, L. G. 1940, PNAS, 26, 50

Holzreuter, R., Fluri, D. M., & Stenflo, J. O. 2005, A&A, 434, 713

House, L. L. 1971, in IAU colloq. 53, Solar Magnetic Fields, ed. R. Howard, 130

Hubeny, I. 1985, in Progress in Stellar Line Formation Theory, ed. J. E. Beckman & L. Crivellari (Dordrecht: Reidel), 27

Hummer, D. G. 1962, MNRAS, 125, 1

Lamb, F. K., & ter Haar, D. 1971, Phys. Rep., 2C, 253

Landi Degl'Innocenti, E. 1983, Sol. Phys., 85, 3

Landi Degl'Innocenti, E. 1984, Sol. Phys., 91, 1

Landi Degl'Innocenti, E., Landi Degl'Innocenti, M., & Landolfi, M. 1997, in Proc. 'Forum THÉMIS', Science with THÉMIS, ed. N. Mein, & S. Sahal-Bréchot (Paris Observatory Publ.), 59

Lin, H., Penn, M. J., & Kuhn, J. R. 1998, ApJ, 493, 978

Lin, H., & Casini, R. 2000, ApJ, 542, 528

Mihalas, D. 1978, Stellar Atmospheres (2nd ed.; Freeman)

Nagendra, K. N. 1994, ApJ, 432, 274

Nagendra, K. N., Paletou, F., Frisch, H., & Faurobert-Scholl, M. 1999, in Proc. of 2nd SPW, ASSl 243, Solar Polarization, ed. K. N. Nagendra, & J. O. Stenflo (Kluwer Academic Publishers), 127

Nagendra, K. N., Frisch, H., & Faurobert, M. 2002, A&A, 395, 305

Nagendra, K. N. 2003, in ASP Conf. Ser. 288, Stellar Atmosphere Modeling, ed. Ivan Hubeny, Dimitri Mihalas, & Klaus Werner (Astronomical Society of the Pacific), 583

Nagendra, K. N., Frisch, H., & Fluri, D. M. 2003, in Proc. of 3rd SPW, ASP Conf. Ser. 307, Solar Polarization, ed. J. Trujillo Bueno, & J. Sánchez Almeida (Astronomical Society of the Pacific), 227

Omont, A., Smith, E. W., & Cooper, J. 1972, ApJ, 175, 185

Omont, A., Smith, E. W., & Cooper, J. 1973, ApJ, 182, 283

Saliba, G. J. 1985, Sol. Phys., 98, 1

Stenflo, J. O. 1994, Solar Magnetic Fields (Dordrecht: Kluwer Academic Publishers)

Stenflo, J. O. 1996, in Proc. of 1st SPW, Solar Polarization, ed. J. O. Stenflo, & K. N.
    Nagendra, also Sol. Phys., 164, 1

Stenflo, J. O. 1998, A&A, 338, 301

Stenflo, J. O. 2006, in Proc. 4th SPW, ASP Conf. Ser., Solar Polarization, ed. R. Casini, &
    B. W. Lites (Astronomical Society of the Pacific), in press

Stenflo, J. O., & Keller, C. U. 1996, Nature, 382, 588

Stenflo, J. O., & Keller, C. U. 1997, A&A, 321, 927

Streater, A., Cooper, J., & Rees, D. E. 1988, ApJ, 335, 503

Trujillo Bueno, J. 2003, in ASP Conf. Ser. 288, Stellar Atmosphere Modeling, ed. Ivan
    Hubeny, Dimitri Mihalas, & Klaus Werner (Astronomical Society of the Pacific), 551

Uitenbroek, H. 2003, in ASP Conf. Ser. 288, Stellar Atmosphere Modeling, ed. Ivan Hubeny,
    Dimitri Mihalas, & Klaus Werner (Astronomical Society of the Pacific), 551

Wallace, L., & Yelle, R. V. 1989, ApJ, 346, 489.

Weisskopf, V. 1933, Observatory, 56, 291

Wooley, R. 1938, MNRAS, 98, 624

Zanstra, H. 1941, MNRAS, 101, 273